A New Model for Barberton Komatiites: Deep Critical Melting with High Melt Retention

CHRISTOPHE C. M. ROBIN-POPIEUL[1], NICHOLAS T. ARNDT[1]*, CATHERINE CHAUVEL[1], GARY R. BYERLY[2], ALEXANDER V. SOBOLEV[1] AND ALLAN WILSON[3]

[1]ISTERRE, UMR 5275 CNRS, UNIVERSITÉ DE GRENOBLE, 38400 SAINT-MARTIN D'HÈRES, FRANCE
[2]LOUISIANA STATE UNIVERSITY, BATON ROUGE, LA 70802, USA
[3]UNIVERSITY OF WITSWATERSRAND, 2000 JOHANNESBURG, SOUTH AFRICA

The oldest well-preserved komatiites, and the type examples, are found in the Barberton Greenstone Belt in South Africa (3·5–3·3 Ga). All three komatiite types are present, commonly within the same stratigraphic unit. Al-depleted komatiites have low Al/Ti, relatively high concentrations of incompatible elements and depleted heavy rare earth elements (HREE); Al-undepleted komatiites have chondritic Al/Ti and flat HREE patterns; and Al-enriched komatiites have high Al/Ti, low concentrations of incompatible elements, enriched HREE and extremely depleted light rare earth elements. Based on a comprehensive petrological and geochemical study, we propose a new melting model for the formation of these magmas. The basis of the model is the observation, from published experimental studies, that at great depths ($\sim$13 GPa) the density of komatiitic liquid is similar to that of solid peridotite. At such depths, melting in a rising mantle plume produces near-neutrally buoyant komatiite melt that does not escape from the residual peridotite. As the source ascends to shallower levels, however, the pressure decreases and the density difference increases, eventually making melt escape possible. Al-depleted komatiites form first at about 13 GPa by equilibrium melting under conditions in which a large proportion of melt (30–40%) was retained in the source and the residue contained a high proportion of garnet (15%). Al-undepleted and Al-enriched komatiites form by fractional melting at intermediate to shallow depths after the escape of a large proportion of melt and after exhaustion of residual garnet. This model reproduces the chemical characteristics of all komatiite types in the Barberton belt and can probably be applied to komatiites in other parts of the world.

KEY WORDS: *Archean; Barberton; komatiite; critical melting; petrogenesis*

INTRODUCTION

Komatiites are thought to result from high degrees of mantle melting (over 30%; Sun & Nesbitt, 1978; Herzberg, 1992), at great depths (down to $\sim$400 km; Herzberg, 1992), under conditions that, apart from one exception (the Cretaceous komatiites from Gorgona Island; Echeverría, 1980), have not existed since the Precambrian. They are usually classed into three types (Sun & Nesbitt, 1978; Jahn *et al.*, 1979, 1982; Nesbitt *et al.*, 1979): (1) Al-depleted or Barberton-type komatiites with sub-chondritic Al_2O_3/TiO_2 ratios and depletion of the heavy rare earth elements (HREE); (2) Al-undepleted or Munro-type komatiites with near primitive-mantle Al_2O_3/TiO_2 ratios of around 22 and flat HREE patterns; (3) Al-enriched komatiites with high Al_2O_3/TiO_2 ratios between 30 and 60 and enrichment of HREE. Herzberg *et al.* (2010) showed that komatiites cannot have been produced by melting of the ambient mantle because this process produces melts with lower MgO contents. Green (1975), Ohtani (1984), Campbell *et al.* (1989), Ohtani *et al.* (1989), Nisbet *et al.* (1993) and Arndt (2003) proposed instead that Al-depleted komatiites were produced in unusually hot mantle plumes by deep ($\sim$400 km), high-degree ($\sim$30%),

*Corresponding author. E-mail: arndt@ujf-grenoble.fr

equilibrium melting at depths where garnet is a stable residual phase. According to Sun & Nesbitt (1978), Herzberg & Ohtani (1988), Ohtani *et al.* (1989) and Kareem (2005), Al-undepleted and Al-enriched komatiites are also produced in mantle plumes, but by shallower melting leaving a garnet-free residue. Al-depleted komatiites are common in the Early Archean and are progressively replaced by Al-undepleted and Al-enriched komatiites in the late Archean, Proterozoic and Phanerozoic (e.g. Nesbitt *et al.*, 1982; Herzberg, 1995; Arndt *et al.*, 2008).

Allègre (1982), Grove *et al.* (1999) and Parman *et al.* (2001, 2004) have proposed an alternative, wet-melting model that explains the generation of komatiites by shallow-level hydrous melting of the mantle wedge above a subduction zone. This model is based, to a large degree, on a questionable interpretation of the Barberton komatiites as intrusive rocks, and it fails to explain the contrasting geochemical characteristics of the three types of komatiite (Arndt *et al.*, 1998, 2008) and the low water contents measured in melt inclusions (McDonough & Ireland, 1993; Shimizu *et al.*, 2001; Berry *et al.*, 2008). Inoue *et al.* (2000) proposed that Al-depleted komatiites could have formed in hydrous mantle plumes.

The komatiites of the Barberton Greenstone Belt are the oldest known well-preserved examples of this type of rock, and the belt is the type area of Al-depleted komatiite. Here we present a comprehensive petrological and geochemical study of a new set of komatiite samples from formations spanning the 200 Myr volcanic history of the belt, our goal being to better constrain the nature of their mantle sources and the origin of this remarkable type of magma.

GEOLOGICAL BACKGROUND

The 3·5–3·2 Ga Barberton Greenstone Belt is located in northeastern South Africa and Swaziland. It forms part of the Archean Kaapvaal craton, the central nucleus of the continent that formed and stabilized between *c.* 3·5 and 3·0 Ga (de Wit *et al.*, 1992). The 12 km thick sequence of metavolcanic and metasedimentary rocks comprises the lower, 9 km thick, mainly volcanic Onverwacht Group overlain by the 3 km thick mainly sedimentary Fig Tree and Moodies Groups. The greenstone belt has been deformed into NE–SW-trending anticlines and synclines (Fig. 1; Lowe *et al.*, 2007). Although almost all strata are sub-vertical, penetrative deformation is rare except in shear zones, and primary textures and structures are preserved. The belt is surrounded by granitoid plutons.

Well-preserved komatiites occur at four levels in the belt (Fig. 1): (1) the 3·48 Ga Komati Formation (Viljoen & Viljoen, 1969a, 1969c; Dann, 2000, 2001); (2) the 3·47 Ga Hooggenoeg Formation (Viljoen & Viljoen, 1969b; Armstrong *et al.*, 1990; Byerly *et al.*, 1996); (3) the 3·3 Ga Mendon Formation (Byerly *et al.*, 1996; Byerly, 1999);

(4) the 3·3 Ga Weltevreden Formation (Lahaye *et al.* 1995; Kareem, 2005; Cooper, 2008).

Komatiites also occur in the older Sandspruit and Theespruit Formations, which underlie the Komati Formation, but these komatiites are too highly metamorphosed and deformed for reliable petrographic and geochemical study. The Komati, Hooggenoeg and Mendon Formations occur in a continuous stratigraphic sequence in the main part of the belt, whereas the Weltevreden Formation occurs in a different block to the north, separated from the southern part by the Inyoka and Moodies faults.

The Komati Formation is composed of a succession of komatiite, komatiitic basalt and tholeiitic basalt flows without inter-flow sedimentary layers or erosion surfaces; the lack of such features indicates that the flows erupted rapidly without major breaks in volcanic activity. The lower Komati Formation is about 1·8 km thick, limited down-section by the Komati fault (Fig. 1) and composed of 50% komatiites and 50% komatiitic basalts. Dann (2000) mapped the unit in detail and identified five spinifex komatiite horizons. Only the lowermost—spinifex horizon 1—has been shown to contain Al-undepleted komatiites (Al_2O_3/TiO_2 from 17 to 23; Williams & Furnell, 1979; Parman *et al.*, 2003, 2004) whereas the rest contains only Al-depleted komatiite (Al_2O_3/TiO_2 from 8 to 12; Viljoen & Viljoen, 1969; Smith *et al.*, 1980; Jahn *et al.*, 1982; Smith & Erlank, 1982; Viljoen *et al.*, 1983; Lahaye *et al.*, 1995; Parman *et al.*, 2003, 2004). The 1·27 km thick upper Komati Formation is limited up-section by the Middle Marker (a thin unit of silicified volcanoclastites) and is composed of komatiitic basalts with minor komatiite and tholeiitic basalt. Komatiites and komatiitic basalts from the upper Komati Formation are exclusively of the Al-depleted type (Al_2O_3/TiO_2 from 10 to 16; Viljoen & Viljoen, 1969a; Jahn *et al.*, 1982; Viljoen *et al.*, 1983; Parman *et al.*, 2003).

The 3·47–3·41 Ga Hooggenoeg Formation overlies the Komati Formation. Lowe & Byerly (1999) divided it into six members (H1–H6), each comprising a volcanic sub-unit capped by a thin unit of silicified sediments indicative of breaks in volcanic activity. The volcanic succession is composed mainly of tholeiitic basalts, but members H3 and H4 also contain komatiitic basalts. These lavas have been shown to belong to the Al-depleted and Al-enriched types (Al_2O_3/TiO_2 of ∼12 and ∼50, respectively; Viljoen & Viljoen, 1969c). The H6 magmatic member is made of felsic rocks.

South of the Inyoka fault, the ∼3·3 Ga Mendon Formation overlies the Kromberg Formation. It is divided into five members (M1–M5), each composed of a volcanic unit capped by a chert layer. All three komatiite types (Al-depleted, Al-undepleted and Al-enriched) occur in each volcanic member (Lahaye *et al.*, 1995; Byerly, 1999).
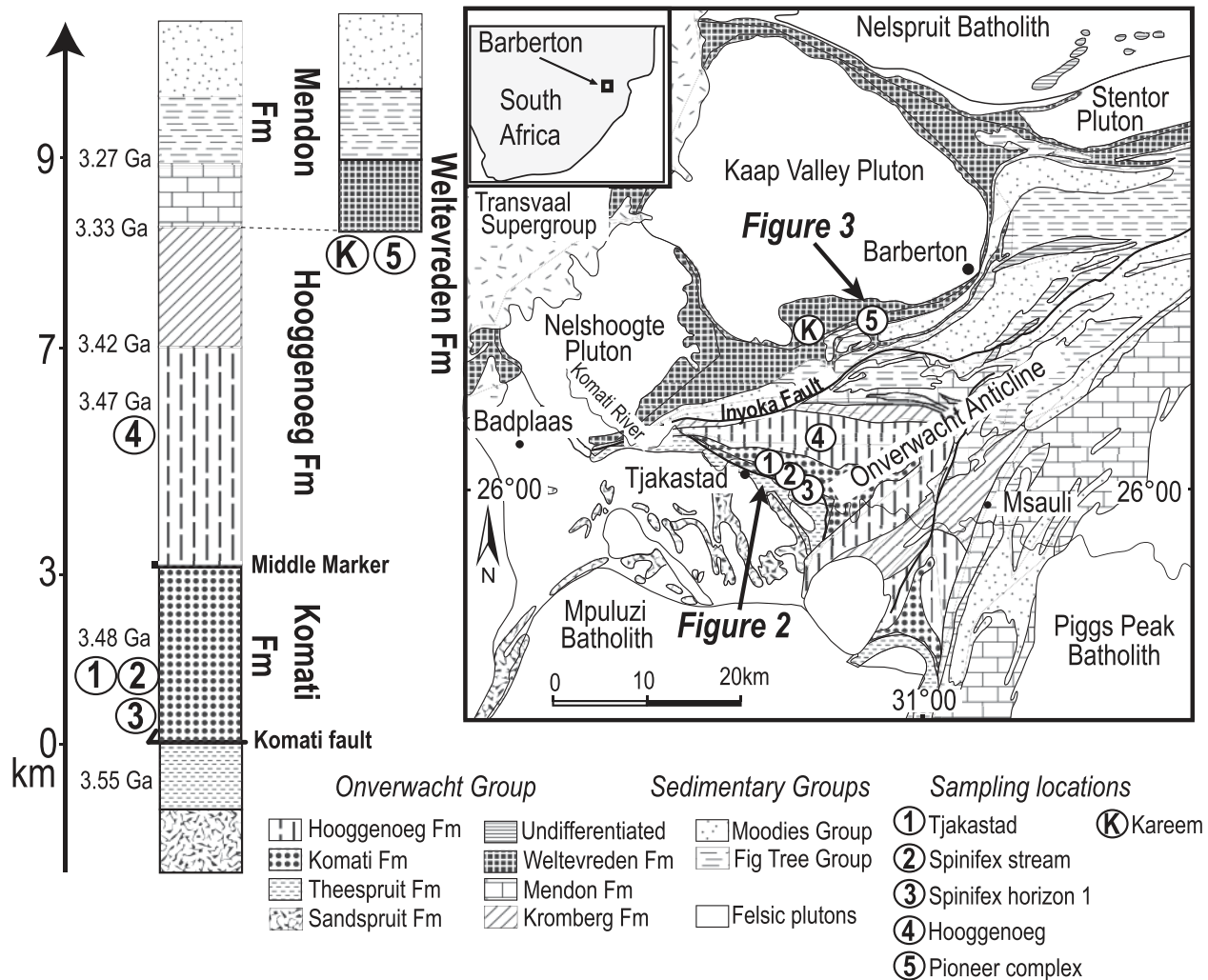
Fig. 1. Geological map and stratigraphic column of the Barberton Greenstone Belt. Map modified from Hofmann (1988). Ages from Armstrong *et al.* (1990) and Byerly *et al.* (1996).

The ~3·3 Ga Weltevreden Formation is thought to be correlative with the upper cycles of the Mendon Formation (Lowe & Byerly, 1999). Komatiitic flows, sills and tuffs account for ~80% of the unit (G. Byerly, personal communication). Almost all komatiites from the Weltevreden Formation are Al-enriched (Al_2O_3/TiO_2 ~30; Kareem, 2005; Cooper, 2008); however, two flows of Al-undepleted komatiite (Al_2O_3/TiO_2 ~22) have been identified. Komatiitic tuffs, which are abundant compared with the other formations, include all three groups of komatiite (Stiegler *et al.*, 2008, 2010).

SAMPLES

We studied 71 samples of komatiite and komatiitic basalt from three formations—Komati, Hooggenoeg and Weltevreden—at five localities. Sample sites and brief descriptions are given in Fig. 1 and Supplementary Data: Electronic

Appendix 1 (available for downloading at http://www.petrology.oxfordjournals.org).

Field characteristics
Komati Formation
Samples of the Komati Formation come from three sites, referred to here as 'Tjakastad', 'Spinifex Stream' and 'Spinifex horizon 1' (Fig. 2).

Tjakastad. Our main sampling site for the Komati Formation is a 250 m thick sequence of komatiites and komatiitic basalts located 1 km NE of Tjakastad townsite and just north of the Komati River (locality 1 in Figs 1 and 2). The lowest exposed unit (labeled 'tumulus' in Fig. 2c) is a thick komatiite unit with very unusual texture and structure. This unit, described as an inflated flow or tumulus structure by Dann (2000, 2001), is composed of a basal adcumulus dunite consisting of tightly packed,
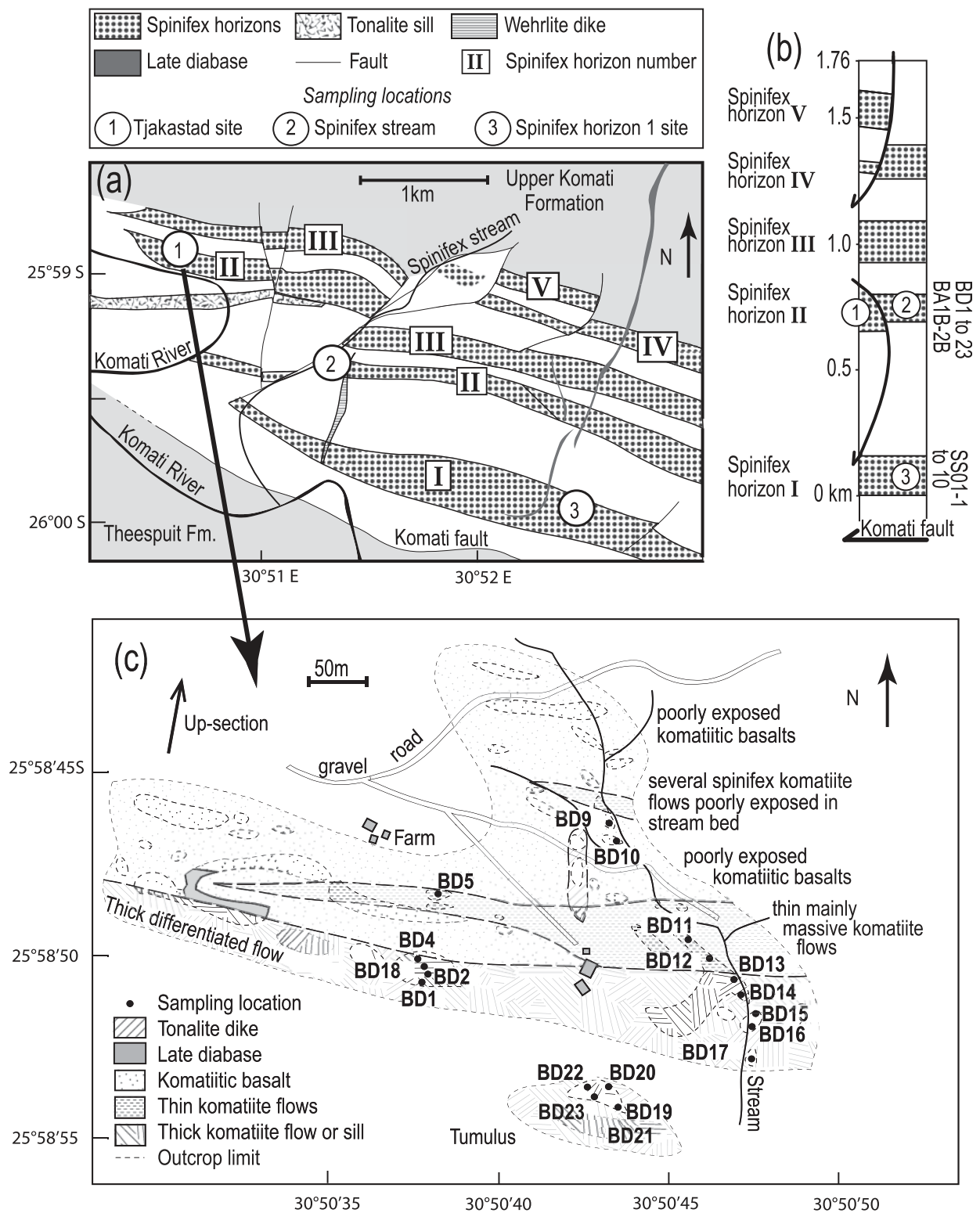
Fig. 2. Map of the Lower Komati Formation and sampling locations. (a) Geological map adapted from Dann (2000). (b) Stratigraphic column after Dann (2000). (c) Detailed outcrop map of sampling location 1 with sample positions.

euhedral, unusually coarse olivine grains (1–2 mm) overlain by a megacrystic wehrlite layer and in turn by a vesicular layer. All olivine grains are totally serpentinized.

The following unit (labeled 'thick differentiated flow' in Fig. 2c) is a 15 m thick differentiated komatiite flow or sill made up of an olivine cumulate layer containing large clinopyroxene oikocrysts, a thick B1 zone [as defined by Pyke *et al.* (1973)] and a well-developed olivine spinifex layer. An unusual feature is pronounced horizontal layering in the upper part of the olivine cumulate. The same unit crops out in the stream in the east of the map area, and there pyroxene spinifex takes the place of olivine spinifex. Next comes a series of thin (1–3 m), mainly massive komatiite flows followed by a series of thicker (∼10 m) komatiitic basalt flows and finally several thin komatiite flows with well-developed olivine spinifex layers interlayered with the komatiitic basaltic units.

Spinifex Stream. At the second site (locality 2 in Figs 1 and 2a), we sampled a thick differentiated unit that is possibly correlative with the thick differentiated unit overlying the tumulus unit in the Tjakastad locality. As in the streambed at the Tjakastad site, pyroxene spinifex is present at the top of the unit. The texture grades from a thin upper zone of acicular pyroxene down to coarse 'string-beef' pyroxene spinifex. The lower part of the flow is an olivine orthocumulate.

Spinifex horizon 1. This site is located about 2 km SE of 'Spinifex Stream' in the lowermost spinifex horizon 1 (Dann, 2000) of the Komati Formation (locality 3 in Figs 1 and 2a). There we sampled several massive and olivine-spinifex textured komatiite flows.

Hooggenoeg Formation

Our samples from the Hooggenoeg Formation come from a site about 6 km north of the Komati Formation sampling locations (locality 4 in Fig. 1). They comprise pyroxene spinifex lava and olivine and pyroxene cumulates from successive flows of komatiitic basalt and komatiite.

Weltevreden Formation

Pioneer Complex. Our samples from the Weltevreden Formation come from the 'Pioneer Complex' (locality 5 in Fig. 1; Wuth, 1980; Anhaeusser, 1985), which is located about 2 km west of the Pioneer gold mine. From the lower half of the complex, we sampled four shallow-level sills or flows that crop out over long distances along strike and are separated by thick (10–50 m) units of ultramafic tuff (Cooper, 2008; Stiegler *et al.*, 2010): WP1 and WP4 (Fig. 3) are thick (90 and 25 m) massive peridotitic and dunitic komatiite units; WP2 and WP3 are thick (50 and 100 m) komatiite units, highly variable along strike and strongly differentiated from a lower olivine cumulate layer, to an intermediate poikilitic to equant pyroxenite layer, and to an upper layer of oriented to random pyroxene spinifex.

Two additional samples were taken in poorly exposed and less laterally variable flows or sills from the upper Pioneer Complex: WP7l and WP7u (Fig. 3). These two units are overlain and underlain by thin (5–10 m), commonly discontinuous, ultramafic tuffs. WP7l is a thick (60 m) massive peridotitic komatiite unit whereas WP7u is a thick (25 m) pyroxene spinifex-bearing unit.

We sampled in detail WP3, which is one of the lowest units in the sequence. This intrusive unit is 75 m thick and is differentiated from a basal 10 m thick dunite layer overlain by a thick (50 m) olivine orthocumulate layer. The upper 15 m of the unit is composed of a pyroxene oikocrystic cumulate succeeded by pyroxene spinifex protrusions into the overlying tuff. These protrusions are ∼5 m wide and ∼10 m long and they are perpendicular to the contact between the flow and the overlying tuff. Only their upper part contains pyroxene spinifex, their base being composed of medium-grained pyroxenite. The pyroxene spinifex is coarse grained with pyroxene needles up to 5 cm long. The tuff is uniform, very fine grained and has been indurated along its contact with the sill. The presence of pyroxene spinifex instead of olivine spinifex shows that the parental lava was a low-MgO komatiitic liquid or a komatiitic basalt. However, the olivine cumulate layers are very thick (∼60 m), indicating extensive olivine accumulation.

One outcrop of unit WP1 is a small hummock of unusually hard, brittle, dark blue–grey olivine cumulate. Thin sections of this material show that it is only slightly altered and contains a high proportion of non-serpentinized magmatic olivine. Samples MC6-4 and WP109 come from this outcrop (Fig. 3).

All these flows were mapped and thoroughly described by Cooper (2008).

Western Weltevreden locality. Kareem (2005) sampled and studied rocks from another part of the Weltevreden Formation (locality K in Fig. 1) at the junction between the roads from Barberton to Nelshoogte and Montrose farms at 25°50·7′S, 30°53·1′E. She studied two continuous sequences of ∼20 m thick flows that are differentiated into upper spinifex and lower cumulate zones. In contrast to the Pioneer Complex, the spinifex is of the olivine variety and the cumulates are dominated by olivine. In her sampling area, only one tuff layer is present, as opposed to the numerous tuffs interlayered between each flow in the Pioneer Complex.

Petrography

In all Barberton komatiites, the primary magmatic minerals are (in crystallization order) olivine, chromite, in some cases orthopyroxene, pigeonite and augite (Viljoen & Viljoen, 1969*b*; Parman *et al.*, 1997; Kareem, 2005). Except
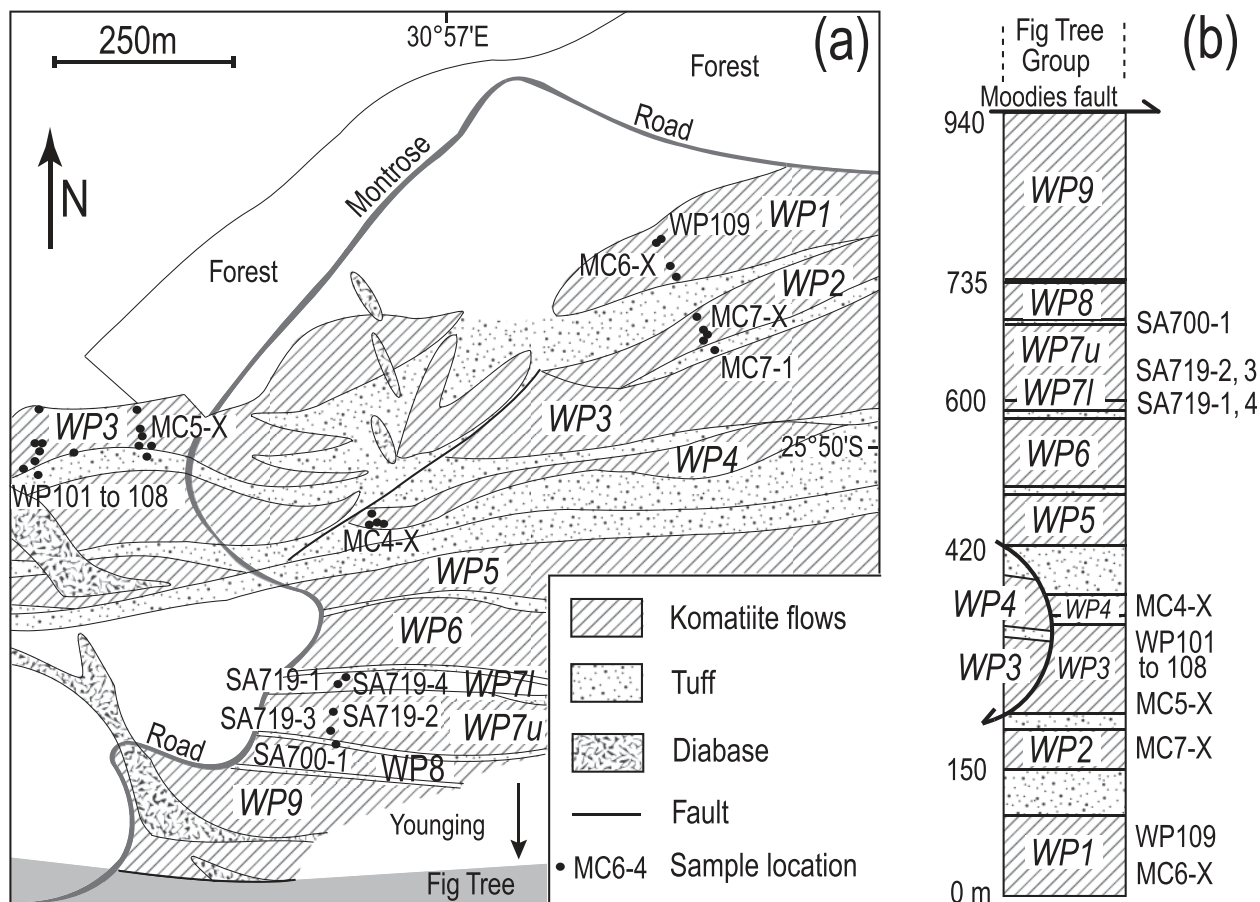
Fig. 3. Geological map and stratigraphy of the Weltevreden Formation, Pioneer Complex. (a) Map, adapted from Cooper (2008), with sampling locations. (b) Stratigraphic column adapted from Cooper (2008). In italic: unit labels; in normal font: sample labels.

for samples in shear zones, textures are well preserved but the primary minerals have been extensively replaced by secondary phases(Viljoen & Viljoen, 1969c). Olivine is usually replaced by chlorite or serpentine and magnetite; orthopyroxene is partially to completely altered to bastite; clinopyroxene is partially to completely replaced by tremolite, chlorite and magnetite; chromite is partially altered to magnetite; and glass has been totally altered to chlorite, tremolite and magnetite. Olivine is preserved in some samples, notably from the Komati and Weltevreden Formations. Detailed descriptions of the state of preservation and textures are given in Supplementary Data: Electronic Appendix 2.

ANALYTICAL TECHNIQUES

Concentrations of major elements in whole-rocks were determined by inductively coupled plasma atomic emission spectroscopy (ICP-AES) using a Perkins-Elmer 3000DV in the Institut des Sciences de la Terre (ISTerre) in Grenoble. Samples (50 g) were dissolved in a mixture of 14N distilled HNO_3 and concentrated HF at 80°C for 24 h in closed Savillex beakers. H_3BO_3 was added to the

solutions to complex the F^- ions. The sample solutions were then diluted in 250 ml of mQ water to be run on the ICP-AES system. Accuracy for major elements is within ±2%, except for Na_2O (5%), K_2O (10%) and P_2O_5 (20%). Detection limits are of the order of 0·1 wt %. The concentrations measured for international standards are reported in Tables 1 and 2. Further details of this method have been given by Chauvel et al. (2011).

Trace elements were analysed by inductively coupled plasma mass spectrometry (ICP-MS) using an Agilent 7500CE quadrupole ICP-MS system also at ISTerre. Samples (100 mg) were dissolved in steel-jacketed Teflon bombs in a mixture of ultrapure concentrated $HClO_4$ and distilled 24N HF for 5 days at 140°C. The fluorides formed were broken using distilled 7N HNO_3 and evaporated. After addition of the spike, the samples were dissolved in distilled 2% HNO_3 + distilled HF (a few drops per liter) and run on the quadrupole ICP-MS system. Accuracy is better than 5% and, for most elements including REE, detection limits are below 0·01 ppm.

Major- and trace-element concentrations for samples BA1-B and BA2-B were provided by Dr Iain Pitcairn from

Table 1: Major-element concentrations (wt %) for standards

Standard:	BEN (Govindaraju, 1994)	BR24 (Blais et al., 2000)	UB-N (Govindaraju, 1994)	BIR-1 (Govindaraju, 1994)	AGV-1 (Govindaraju, 1994)	BHVO-2 (Plumlee, 1998)	BEN (n = 2)	σ BEN	BR24 (n = 3)	σ BR24	UB-N (n = 4)	σ UB-N	BIR-1 (n = 2)	σ BIR-1	AGV1	BHVO-2
SiO_2	38·20	46·20	39·43	47·70	58·80	49·90	38·4	0·61	46·2	0·28	39·5	0·32	47·3	0·002	58·5	49·4
TiO_2	2·61	2·96	0·11	0·97	1·05	2·73	2·57	0·04	3·04	0·11	0·10	0·01	0·93	0·03	1·00	2·72
Al_2O_3	10·07	13·60	2·90	15·4	17·2	13·5	10·1	0·14	13·7	0·28	2·40	0·23	15·5	0·07	17·0	13·5
$Fe_2O_{3\ tot}$	12·84	12·50	8·34	11·3	6·77	12·3	12·8	0·16	12·9	0·35	8·20	0·16	11·3	0·04	7·26	12·2
MnO	0·20	0·16	0·12	0·18	0·10	0·17	0·20	0·003	0·17	0·001	0·12	0·0005	0·17	0·0004	0·10	0·17
MgO	13·15	9·60	35·21	9·70	1·53	7·23	13·3	0·29	9·83	0·06	35·1	0·28	9·57	0·16	1·41	7·14
CaO	13·87	9·40	1·20	13·4	4·94	11·4	14·0	0·24	9·59	0·10	1·17	0·05	13·2	0·01	4·89	11·4
Na_2O	3·18	3·06	0·10	1·81	4·26	2·22	3·18	0·02	3·01	0·07	0·11	0·01	1·79	0·01	4·18	2·18
K_2O	1·39	0·76	0·02	0·03	2·92	0·52	1·39	0·002	0·75	0·02	–	–	–	–	2·87	0·50
P_2O_5	1·05	0·45	0·04	0·03	0·49	0·27	1·08	0·06	0·46	0·08	–	–	–	–	0·52	0·08
Cr_2O_3	–	–	–	–	–	–	–	–	0·07	–	0·30	–	–	–	–	–
NiO	–	–	–	–	–	–	–	–	0·05	–	0·25	–	–	–	–	–
LOI	2·45	0·71	–	–	–	–	2·94	–	0·62	–	–	–	–	–	–	–
Total	99·01	99·40	87·47	100·52	98·06	100·24	99·9		100·0		86·8		99·8		97·8	99·3

BEN, BR24, UB-N and a diluted artificial 1000 ppm Chem-lab standard were used as calibration standards. When multiple analyses were performed on the same standard, an average is presented here. In this case, *n* is the number of analyses and δ the standard deviation on the concentrations. Iron is reported as Fe_2O_3 total iron. Measured concentrations for BEN, BR24 and UB-N are given for the series of analyses in which they were not used as calibration standards. –, not determined.

Table 2: Trace-element concentrations (ppm) for standards

Standard:	BHVO-2	BIR-1 (n = 5)	σ BIR-1	UBN (n = 3)	σ UBN	PCC1 (n = 2)	σ PCC1	BR24	DTS2b	BEN	RGM1
Li	4·80	3·44	0·145	31·6	4·81	–	–	–	1·91	–	63·1
Sc	32·0	42·6	1·07	13·7	1·63	–	–	–	3·04	–	4·99
Ti	16300	5510	135	606	75·7	–	–	–	46·7	–	1510
V	317	312	6·11	67·2	8·41	–	–	–	21·5	–	10·8
Cr	280	367	14·8	2280	220	3550	40·3	–	14300	–	2·52
Co	45·0	50·5	1·68	102	13·5	152	2·83	52·6	130	59·7	1·96
Ni	119	161	2·65	1930	211	–	–	–	3240	–	–
Cu	127	112	1·73	25·1	2·69	–	–	–	3·33	–	10·8
Zn	103	67·3	0·854	90·3	9·55	–	–	–	50·2	–	34·2
As	0·87	0·33	0·0552	9·74	0·933	–	–	–	0·307	–	3·01
Rb	9·11	0·304	0·114	2·83	0·581	0·109	0·0106	81·0	0·0379	45·7	160
Sr	396	107	3·29	8·01	1·18	0·598	0·00636	622	0·538	1390	115
Y	26·0	15·0	0·378	2·69	0·365	0·128	0·000707	28·4	0·0353	28·5	24·1
Zr	172	14·2	0·947	3·96	0·713	3·27	0·0212	289	0·15	268	232
Nb	18·1	0·569	0·109	0·0516	0·00586	0·0411	0·00714	38·7	0·019	118	9·10
Cd	0·06	0·0288	0·000964	0·0133	0·000141	–	–	–	0·00288	–	0·0688
Cs	0·10	0·00584	0·00128	11·9	0·854	0·0035	0·000368	0·632	0·000948	0·735	9·86
Ba	131	6·51	0·121	28·4	2·86	1·41	0·0283	385	11·2	1060	840
La	15·2	0·602	0·0104	0·34	0·0369	0·0353	0·000707	33·4	0·0112	84·7	22·9
Ce	37·5	1·88	0·0182	0·846	0·097	0·079	0·000424	72·5	0·0237	158	46·0
Pr	5·35	0·377	0·00559	0·126	0·0163	0·00912	9·19E–05	9·49	0·00314	17·4	5·34
Nd	24·5	2·38	0·0311	0·636	0·0776	0·0338	0·000849	39·6	0·0153	67·1	19·3
Sm	6·07	1·10	0·0219	0·234	0·0315	0·00602	0·00082	8·25	0·00253	12·0	3·81
Eu	2·07	0·522	0·00709	0·0863	0·00704	0·00143	0·000481	2·60	0·00113	3·65	0·613
Gd	6·24	1·90	0·0365	0·345	0·0348	0·00698	7·07E–06	7·45	0·00472	9·91	3·67
Tb	0·92	0·356	0·00365	0·0635	0·00897	0·00135	0·000431	1·07	0·00112	1·32	0·597
Dy	5·31	2·56	0·0292	0·455	0·0493	0·0115	0·00148	5·70	0·00547	6·43	3·62
Ho	0·98	0·574	0·00488	0·10	0·0102	0·00306	0·000205	1·04	0·00115	1·07	0·759
Er	2·54	1·73	0·0286	0·308	0·03	0·0131	0·000424	2·71	0·0046	2·57	2·32
Tm	–	–	–	–	–	–	–	–	–	–	
Yb	2·00	1·65	0·0286	0·317	0·026	0·0238	7·07E–05	2·12	0·00856	1·85	2·51
Lu	0·274	0·248	0·00456	0·0491	0·00527	0·00476	0·000332	0·296	0·00201	0·239	0·383
Hf	4·36	0·587	0·0267	0·141	0·0172	0·0609	0·000778	6·65	0·00555	5·55	5·77
Ta	1·14	0·0401	0·00167	0·0137	0·00265	0·000924	0·000165	2·35	0·00107	5·59	0·902
Tl	0·03	0·00245	0·000462	0·0607	0·0112	–	–	–	0·000879	–	1·23
Pb	1·60	3·27	0·142	15·3	1·88	8·63	0·0566	3·91	4·04	4·27	24·7
Th	1·22	0·0312	0·00143	0·0799	0·0256	0·012	0·000424	4·79	0·00287	10·7	14·8
U	0·403	0·00987	0·000511	0·0638	0·00935	0·00548	0·000276	1·20	0·0017	2·39	5·34

BHVO-2 is the calibration standard using the trace-element composition reported by Chauvel *et al.* (2011). When multiple analyses were performed on the same standard, an average is presented here. In this case, *n* is the number of analyses and δ the standard deviation on the concentrations. —, not determined.

University of Stockholm. These analyses were performed by Activation Labs (Canada). Major elements were measured using a Fusion ICP-AES Varian Vista 735 ICP system and trace elements using a quadrupole ICP-MS system.

Further details of the analytical method are available on the Activation Labs website (http://www.actlabs.com/).

Olivine compositions were determined using a Jeol JXA 8200 electron microprobe at the Max-Planck Institute of

Chemistry. The samples were crushed and the olivine was separated for analysis. Each olivine grain was analyzed in the center of its fresh kernel with a voltage of 20 kV and a current of 300 nA. We analyzed olivines from seven samples with ∼75 analyses per sample. For trace elements (TiO_2, Al_2O_3, Cr_2O_3, NiO, CaO, MnO and CoO), detection limits are around 6–15 ppm and 2σ errors are 15–30 ppm. For Mg#, the 2σ error is 0·01 mol %. Further information has been provided by Sobolev *et al.* (2007).

All samples are altered and yield ∼10% loss on ignition (LOI). To approximate the compositions of the anhydrous parental magmas, we normalized all major- and trace-element data on a 100% volatile-free basis. FeO and Fe_2O_3 contents were recalculated from total Fe_2O_3 using the method described in Supplementary Data: Electronic Appendix 3.

RESULTS
Whole-rock chemistry
Results are presented in Tables 3 and 4, and in Figs 4–7. To eliminate the effects of olivine accumulation or fractionation, the trace elements were normalized to the MgO content of the parental magma using the method described in Electronic Appendix 3. The compositions of our samples correspond to those presented in earlier publications (Viljoen & Viljoen, 1969a,b; Williams & Furnell, 1979; Smith *et al.*, 1980; Smith & Erlank, 1982; Viljoen *et al.*, 1983; Lahaye *et al.*, 1995; Parman *et al.*, 2003; Kareem, 2005; Cooper, 2008). MgO contents range from high values, up to 45 wt %, in the olivine cumulates, to about 10 wt % in the most evolved spinifex lavas.

Komatiites from the various types and formations are distinguished by their Al_2O_3, TiO_2, FeO and trace-element contents (Fig. 4). Figure 6 shows that the commonly used terms Al-depleted and Al-enriched are somewhat misleading. Most of the difference in the Al_2O_3/TiO_2 ratios is in fact due to differences in TiO_2 contents, which are significantly higher in 'Al-depleted' komatiites than in 'Al-enriched' komatiite. We take into account these differences in our treatment of the data, but believe it is difficult to avoid using these terms, which are well entrenched in the literature and which call attention to the relative Al content of the komatiites. The latter is controlled by the presence or absence of garnet during the melting process and plays a crucial role in our petrogenetic models.

Al-depleted komatiites have low Al_2O_3/TiO_2 ratios of about 12 (Fig. 6) and depleted HREE patterns (Fig. 5a, c and d). Their MgO-normalized trace-element concentrations are higher than those of other types, at around three times primitive mantle values, and they also have relatively high TiO_2 and FeO, and low Al_2O_3 at a given MgO content (Fig. 4a, c and f). This type dominates the Komati Formation and is also found in the Hooggenoeg

Formation. According to Lahaye *et al.* (1995) and Byerly (1999), they also occur in the Mendon Formation. They are all slightly depleted in light REE (LREE), except for five samples from our spinifex horizon 1 sampling site (locality 3 in Figs 1 and 2).

Al-undepleted komatiites have Al_2O_3/TiO_2 ratios close to the primitive mantle value of about 22 (Fig. 6) and flat HREE patterns (Fig. 5e and g). Except for modest LREE depletion, their trace-element spectra are straight and close to horizontal. Their MgO-normalized trace-element concentrations are intermediate between those of the two other types and close to primitive mantle values. They also have intermediate TiO_2, FeO and Al_2O_3 concentrations at given MgO (Fig. 4a, c and f). We found samples of this type in several flows of the Komati, Hooggenoeg, and Weltevreden Formations, and Byerly (1999) described a few occurrences in the Mendon Formation.

Al-enriched komatiites have higher than chondritic Al_2O_3/TiO_2 ratios of around 30 and are HREE enriched (Fig. 5h). Their MgO-normalized trace-element concentrations are lower than those of the other types, being close to or lower than those of the primitive mantle. They also have lower TiO_2 and FeO, and higher Al_2O_3 at a given MgO. This type of komatiite dominates the Weltevreden Formation and also occurs in the Mendon Formation (Byerly, 1999).

In Fig. 7a, Gd/Yb_N is used as an indicator of HREE depletion or enrichment. This figure shows that the three types define an array between an Al-depleted end-member with low Al_2O_3/TiO_2 and depleted HREE and an Al-enriched end-member with high Al_2O_3/TiO_2 and enriched HREE.

Olivine compositions
Olivine compositions in two samples from the Komati Formation (BD6 and BD12) and five from the Weltevreden Formation (MC6-4, MC4-2, MC4-4, WP109 and SA719-1) are reported in Table 5. Komati Formation sample BD6, which was collected in a thick, massive unit with a pyroxene spinifex-textured top, contains olivine with distinctly lower Mg# (86·8–89·4) than in the other samples. The other Komati Formation sample BD12 has slightly lower Mg# (90·8–92·3) than samples from the Weltevreden Formation (91·5–93·7). The olivine analyzed by Kareem (2005) from the Weltevreden Formation has a still higher Mg# of 95·6.

DISCUSSION
Effects of secondary processes: alteration and metamorphism
To investigate the effects of alteration of our komatiite samples and to calculate the compositions of their parental magmas, we used the olivine differentiation trends that are characteristic of komatiites. The very low viscosities of

Table 3: Major-element concentrations (wt %) normalized to 100% on a volatile-free basis

| Formation: | Komati | | | | | | | | | | | | |
| Type: | Al-depleted | | | | | | | | | | | | |
Sample:	BD1	BD2	BD4	BD4dup	BD5	BD6	BD7	BD11	BD12	BD18	BD19	BD20	BD21
SiO_2	45·0	44·2	48·1	48·0	46·5	43·9	53·9	49·8	44·3	45·7	45·1	46·8	44·5
TiO_2	0·22	0·42	0·34	0·34	0·34	0·20	0·61	0·41	0·21	0·20	0·14	0·25	0·14
Al_2O_3	2·2	3·5	3·7	3·7	3·4	2·0	6·6	4·4	2·0	2·0	1·2	2·5	1·3
$Fe_2O_{3\ tot}$	10·2	13·7	12·2	12·1	12·8	12·2	12·4	11·5	10·3	9·3	9·3	11·0	9·7
MnO	0·13	0·17	0·16	0·16	0·18	0·17	0·21	0·20	0·13	0·10	0·09	0·15	0·07
MgO	38·6	32·5	29·7	29·8	30·6	37·4	12·4	23·8	39·3	40·2	42·3	38·5	43·5
CaO	3·2	4·4	5·0	5·1	5·4	3·6	10·6	9·3	3·2	2·0	1·3	0·2	0·1
Na_2O	0·04	0·12	0·31	0·31	0·18	0·03	2·84	0·19	0·04	0·02	<DL	<DL	<DL
K_2O	<DL	0·06	<DL	<DL	<DL	<DL	<DL	<DL	<DL	<DL	<DL	<DL	<DL
P_2O_5	<DL	0·1	<DL	<DL	<DL	<DL	0·2	<DL	<DL	<DL	<DL	<DL	<DL
Cr_2O_3	0·23	0·68	0·29	0·68	0·20	0·20	0·15	0·32	0·23	0·22	0·18	0·26	0·20
NiO	0·27	0·23	0·18	0·23	0·23	0·28	0·04	0·12	0·26	0·29	0·38	0·46	0·36
Total	100·0	100·0	100·0	100·4	100·0	100·0	100·0	100·0	100·0	100·0	100·0	100·0	100·0
LOI	13·2	8·2	8·5	–	7·3	8·1	1·1	7·2	10·3	13·0	14·0	13·1	13·2
Al_2O_3/TiO_2	9·8	8·2	10·9	10·9	10·0	10·0	10·9	10·7	9·7	10·1	8·4	9·8	9·4

| Formation: | Komati | | | | | | | | | | | | |
| Type: | Al-depleted | | | | | | | | Al-undepleted | | | | |
Sample:	BD22	BD23	BA1-B	BA2-B	SS016	SS017	SS018	SS019	SS0110	SS011	SS012	SS013	SS014	SS015
SiO_2	45·8	45·1	47·1	46·9	43·9	44·5	45·3	44·8	46·8	44·8	44·4	45·2	44·2	43·8
TiO_2	0·22	0·17	0·32	0·31	0·23	0·21	0·26	0·22	0·33	0·16	0·14	0·15	0·13	0·12
Al_2O_3	1·8	1·7	3·3	3·2	2·9	2·8	3·2	3·0	3·5	3·2	2·8	3·1	2·6	2·5
$Fe_2O_{3\ tot}$	8·7	11·4	11·5	12·5	11·9	12·0	12·1	12·1	11·8	11·2	10·7	10·8	10·5	10·6
MnO	0·14	0·14	0·18	0·16	0·19	0·18	0·17	0·16	0·17	0·17	0·16	0·15	0·16	0·16
MgO	42·4	40·5	31·3	31·0	37·0	36·8	34·9	36·3	30·9	35·3	37·2	35·8	38·0	38·7
CaO	0·2	0·1	5·4	5·2	2·9	2·6	3·4	2·6	5·7	4·2	3·8	4·0	3·6	3·3
Na_2O	<DL	<DL	0·22	0·13	<DL	<DL	<DL	<DL	0·27	0·12	0·09	0·10	0·06	0·04
K_2O	<DL	<DL	0·04	<DL	<DL	<DL	<DL	<DL	0·06	0·15	0·13	0·09	0·08	0·07
P_2O_5	<DL	<DL	<DL	<DL	<DL	0·2	<DL	<DL	<DL	<DL	<DL	<DL	<DL	<DL
Cr_2O_3	0·21	0·45	0·33	0·33	0·65	0·63	0·60	0·63	0·28	0·37	0·34	0·34	0·33	0·32
NiO	0·53	0·40	0·27	0·33	0·24	0·24	0·22	0·24	0·20	0·26	0·28	0·26	0·28	0·29
Total	100·0	100·0	100·0	100·0	100·0	100·0	100·0	100·0	100·0	100·0	100·0	100·0	100·0	100·0
LOI	13·1	11·8	8·4	8·5	10·2	10·5	9·5	9·8	7·5	8·6	7·6	8·9	7·9	8·0
Al_2O_3/TiO_2	8·3	9·9	10·5	10·2	13·1	13·4	12·4	13·3	10·4	20·5	20·8	20·9	20·8	20·4

Table 3: Continued

Formation:	Weltevreden											
Type:	Al-enriched											Al-depleted
Sample:	MC6-1	MC6-4	MC7-6	MC5-1	MC5-3	MC5-5	MC5-6	MC5-7	MC4-3	MC4-3dup	MC4-4	SA700-1
SiO_2	41·9	44·3	46·9	43·0	43·4	47·1	47·0	48·5	45·2	45·2	43·9	50·5
TiO_2	0·29	0·10	0·17	<DL	0·07	0·24	0·39	0·19	0·09	0·09	0·08	0·26
Al_2O_3	12·3	2·8	5·0	1·3	2·2	6·9	13·3	5·1	2·9	2·9	2·4	2·9
$Fe_2O_{3\ tot}$	11·4	9·2	9·6	5·9	8·1	10·4	9·3	8·2	9·0	8·9	8·6	10·6
MnO	0·19	0·13	0·15	0·20	0·15	0·14	0·18	0·15	0·12	0·12	0·12	0·20
MgO	24·2	40·2	33·3	48·4	43·2	26·5	10·1	31·5	39·7	39·8	42·3	28·5
CaO	9·2	2·6	4·2	0·6	1·6	7·8	19·6	5·3	2·0	2·0	1·8	6·2
Na_2O	0·09	0·03	0·05	<DL	<DL	0·25	0·10	0·41	0·01	0·01	<DL	0·10
K_2O	0·05	<DL	<DL	<DL	<DL	<DL	<DL	<DL	<DL	<DL	<DL	<DL
P_2O_5	<DL	0·2	<DL	<DL	<DL	<DL	<DL	<DL	<DL	<DL	<DL	<DL
Cr_2O_3	0·34	0·14	0·41	0·29	0·94	0·55	0·06	0·43	0·74	0·73	0·60	0·36
NiO	0·09	0·27	0·20	0·39	0·35	0·16	0·02	0·19	0·19	0·19	0·33	0·32
Total	100·0	100·0	100·0	100·0	100·0	100·0	100·0	100·0	100·0	100·0	100·0	100·0
LOI	7·8	9·3	9·7	18·3	14·7	7·5	3·9	8·9	10·9	10·9	9·6	8·0
Al_2O_3/TiO_2	42·7	26·9	29·2	–	33·0	28·3	34·2	27·7	31·8	31·2	30·4	11·3

Formation:	Weltevreden											
Type:	Al-undepleted			Al-enriched								
Sample:	SA719-1	SA719-2	SA719-4	WP101	WP102	WP103	WP104	WP105	WP106	WP107	WP108	WP109
SiO_2	45·4	46·6	45·6	43·2	44·5	43·8	46·7	52·9	53·6	46·6	47·5	44·7
TiO_2	0·14	0·36	0·12	<DL	<DL	0·30	0·12	0·10	0·49	0·14	0·38	0·09
Al_2O_3	3·0	7·1	2·6	1·3	1·4	9·6	3·8	4·0	14·4	4·8	13·0	2·6
$Fe_2O_{3\ tot}$	9·0	11·2	9·1	10·2	6·9	4·7	9·2	8·0	10·4	9·1	9·1	9·0
MnO	0·10	0·16	0·13	0·11	0·11	0·23	0·15	0·10	0·17	0·13	0·17	0·14
MgO	39·0	25·8	41·8	44·3	45·8	15·2	36·2	22·9	6·6	33·3	9·5	40·3
CaO	2·7	8·2	<DL	0·2	0·4	26·0	3·3	11·2	9·3	4·7	20·1	2·5
Na_2O	0·02	0·10	<DL	<DL	<DL	<DL	0·05	0·10	4·84	0·29	0·12	0·02
K_2O	<DL	<DL	<DL	<DL	<DL	<DL	<DL	<DL	0·21	<DL	0·04	<DL
P_2O_5	<DL	<DL	<DL	<DL	0·2	<DL	<DL	<DL	<DL	0·2	<DL	<DL
Cr_2O_3	0·36	0·31	0·33	0·34	0·28	0·17	0·35	0·55	0·01	0·41	0·06	0·42
NiO	0·32	0·08	0·35	0·30	0·35	0·05	0·23	0·17	0·01	0·21	0·02	0·25
Total	100·0	100·0	100·0	100·0	100·0	100·0	100·0	100·0	100·0	100·0	100·0	100·0
LOI	10·9	7·7	13·4	17·5	15·7	4·5	11·0	4·5	2·3	9·2	3·5	8·4
Al_2O_3/TiO_2	21·7	19·7	21·6	–	–	31·5	31·2	38·5	29·0	33·6	34·1	30·1

(continued)

Table 3: Continued

Formation:	Hooggenoeg						
Type:	Al-undepleted				Al-depleted		
Sample:	HOG1	HOG1 dup	HOG2	HOG3	HOG4	HOG5	HOG6
SiO_2	55·8	55·7	53·9	54·0	44·9	43·6	47·2
TiO_2	0·41	0·41	0·43	0·42	0·38	0·22	0·43
Al_2O_3	10·2	10·3	10·7	10·3	4·8	3·0	5·7
$Fe_2O_{3\ tot}$	10·1	10·2	11·4	11·5	14·1	12·2	12·3
MnO	0·18	0·18	0·17	0·20	0·18	0·14	0·13
MgO	10·3	10·4	12·0	11·3	30·5	37·1	23·6
CaO	9·4	9·5	8·6	8·7	4·1	2·4	9·7
Na_2O	2·96	2·97	2·64	3·44	0·09	<DL	0·18
K_2O	0·30	0·31	<DL	0·07	0·09	0·07	<DL
P_2O_5	0·2	<DL	<DL	<DL	<DL	<DL	<DL
Cr_2O_3	0·12	0·12	0·13	0·12	0·61	0·94	0·54
NiO	0·02	0·02	0·02	0·02	0·25	0·33	0·22
Total	100·0	100·0	100·0	100·0	100·0	100·0	100·0
LOI	3·7	3·7	3·4	2·9	9·8	12·3	6·0
Al_2O_3/TiO_2	24·8	24·8	24·7	24·5	12·6	13·9	13·2

Iron is reported as Fe_2O_3 total iron. dup, duplicate. —, not determined. <DL, below detection limit. The total value reported is after normalization; the LOI value is only reported for information.

komatiite liquids, a consequence of their high eruption temperature and ultramafic composition, allow crystals to settle rapidly and accumulate in the lower part of the flows. At surface pressure, olivine is the liquidus mineral (Arndt, 1976), and apart from a small amount of chromite, it is the only mineral to crystallize for most of the crystallization range (Arndt, 1977; Kinzler & Grove, 1985; Kareem, 2005). Subtraction or accumulation of olivine results in olivine control lines in MgO variation diagrams (Electronic Appendix 4). These lines contain a composition representing the parental liquid (i.e. the composition of the lava before it differentiated into olivine-enriched cumulates and olivine-depleted spinifex lavas) and project to the average composition of the accumulated olivine, which is found at the intercept with the x-axis in incompatible element vs MgO diagrams.

To investigate element mobility, we evaluated the disturbances of the data around the olivine control lines. Inspection of Fig. 4 shows that within single units there is negligible to moderate scatter for TiO_2, Al_2O_3 and Zr, which suggests that these elements, as well as MgO, have not been strongly mobilized. On this basis we argue that the concentrations of these elements are close to those in the original magmas. Lanthanum plots on a tight trend in some units but not in others. The REE and high field strength elements (HFSE; Nb, Th, Hf and Y; not shown)

also show only minor scatter. On the other hand, SiO_2, FeO, MnO, Na_2O and the large ion lithophile elements (LILE; Cs, Rb, Ba and Sr) scatter widely, which shows that they were extensively mobilized. CaO plots on a tight trend, except for the least magnesian samples and for cumulates from the Komati Formation, which appear to have lost CaO.

Another way to investigate mobilization of the trace elements is to consider their relative abundances in mantle-normalized diagrams such as Fig. 8. In komatiites from the Komati Formation, for example, the concentrations of LILE, as well as Li, to a lesser extent Eu, and U vary widely and irregularly from one sample another and can be assumed to have been mobile. The REE and HFSE scatter far less and presumably were not mobilized by secondary processes.

Below, we use MgO contents to estimate the eruption temperatures of the komatiite liquids and it is therefore crucial to demonstrate that the concentrations of this element have not been changed significantly by alteration or crystal accumulation. Although the scatter illustrated in diagrams such as Fig. 4 is greater than in better-preserved komatiites such as those from the Belingwe Belt in Zimbabwe (Nisbet *et al.*, 1987) or on Gorgona Island (Kerr *et al.*, 1995), the coincidence between the intercept of the olivine control lines and measured olivine compositions indicates that the

Table 4: Trace-element concentrations (ppm) normalized to 100% on a volatile-free basis

| Formation: | Komati | | | | | | | | | | | | | | | | |
| Type: | Al-depleted | | | | | | | | | | | | | | | | |
Sample:	BD1	BD1dup	BD2	BD2dup	BD4	BD5	BD6	BD7	BD11	BD12	BD18	BD19	BD20	BD21	BD22	BD23	BA1-B	BA2-B
Li	7·26	7·26	5·82	5·77	6·08	3·66	1·68	2·97	25·2	3·85	8·42	3·9	7·18	0·331	1·35	4·87	3·83	3·51
Sc	11·9	11·9	20·7	20·1	18·5	16·8	11·5	31·9	22·4	12·3	11·4	7·75	13·5	8·17	10·7	10·8	17·8	17·2
Ti	1160	1170	2740	2760	1960	1900	1080	3510	2390	1090	1080	708	1340	670	1200	956	1880	1840
V	65·9	66·2	144	144	110	104	67·0	194	133	64·5	60·7	36·4	68·5	45·4	53·7	55·6	80·6	85·9
Cr	1590	1620	4700	4730	2040	3370	2420	1060	2200	1600	1530	1250	1780	1400	1410	3130	2250	2250
Co	112	112	155	156	105	112	132	63·1	92·9	116	110	127	119	125	122	128	120	120
Ni	2140	2130	1830	1860	1430	1420	1770	352	948	2060	2280	3020	3690	2840	4210	3190	2120	2590
Cu	3·29	3·54	52·8	57·1	15·9	31·2	29·4	114	58·5	26·0	3·00	1·46	5·52	1·90	3·42	9·46	23·6	47·8
Zn	55·6	56·1	82·3	84·5	73·5	78·9	68·0	71·5	73·9	49·9	54·8	46·9	81·3	43·9	48·0	69·2	78·2	73·0
As	1·77	1·73	0·466	0·702	0·963	0·839	0·592	0·463	0·431	0·207	2·86	2·02	0·83	1·28	1·43	1·72	–	–
Rb	1·08	1·07	2·25	1·50	0·991	0·996	0·367	0·563	0·175	0·605	0·686	0·158	0·266	0·294	0·175	0·469	0·491	0·546
Sr	49·4	49·6	14·7	14·2	20·2	21·9	9·00	45·1	55·2	3·45	36·4	22·0	3·45	1·04	4·94	3·88	29·2	34·7
Y	4·70	4·73	8·28	8·18	7·87	7·47	3·98	12·9	7·32	3·70	4·40	2·36	3·74	2·84	5·21	3·24	6·82	6·96
Zr	13·9	13·9	30·0	30·0	23·8	23·3	11·8	38·3	23·9	10·9	12·8	7·04	15·4	7·14	11·9	11·1	21·2	21·2
Nb	0·857	0·859	0·819	0·827	1·41	1·21	0·632	2·05	1·23	0·54	0·751	0·453	0·976	0·444	0·846	0·658	1·37	1·27
Cd	0·00842	0·00873	0·023	0·0228	0·0207	0·0202	0·017	0·0291	0·0259	0·00886	0·00651	0·0071	0·0216	0·00384	0·00883	0·00953	–	–
Cs	0·694	0·698	0·51	0·549	0·761	0·524	0·142	0·034	0·0698	0·229	0·442	0·027	0·166	0·0202	0·0369	0·134	0·0957	0·0887
Ba	15·3	15·3	52·7	54·3	7·84	13·7	0·691	9·25	2·92	2·37	16·7	5·08	13·9	8·23	5·80	31·2	4·44	5·34
La	1·18	1·16	1·00	0·986	1·90	1·49	0·818	3·17	1·65	0·677	0·988	0·513	0·713	0·687	1·03	0·675	1·60	1·76
Ce	3·19	3·18	2·84	2·90	5·14	3·96	2·29	7·94	3·45	1·88	2·58	1·46	3·92	1·79	2·48	2·06	4·24	4·54
Pr	0·474	0·473	0·49	0·490	0·775	0·644	0·360	1·23	0·695	0·297	0·404	0·217	0·354	0·285	0·463	0·308	0·689	0·75
Nd	2·31	2·34	2·87	2·82	3·78	3·23	1·84	6·12	3·67	1·55	2·06	1·12	1·62	1·40	2·30	1·51	3·44	3·65
Sm	0·686	0·685	1·15	1·14	1·16	0·985	0·558	1·86	1·17	0·528	0·582	0·327	0·642	0·39	0·634	0·509	0·993	1·10
Eu	0·239	0·242	0·448	0·424	0·476	0·344	0·192	0·72	0·232	0·189	0·249	0·131	0·291	0·139	0·177	0·159	0·351	0·402
Gd	0·805	0·803	1·55	1·59	1·36	1·27	0·708	2·28	1·45	0·641	0·737	0·408	0·749	0·469	0·804	0·59	1·25	1·34
Tb	0·130	0·129	0·263	0·266	0·242	0·217	0·122	0·382	0·224	0·106	0·125	0·0651	0·151	0·0728	0·124	0·105	0·206	0·22
Dy	0·883	0·881	1·66	1·66	1·46	1·42	0·770	2·45	1·45	0·709	0·789	0·424	1·03	0·512	0·796	0·676	1·34	1·41
Ho	0·177	0·177	0·324	0·333	0·304	0·300	0·156	0·504	0·284	0·143	0·163	0·0893	0·196	0·105	0·166	0·142	0·27	0·289
Er	0·505	0·507	0·893	0·907	0·868	0·837	0·438	1·42	0·796	0·412	0·478	0·255	0·592	0·297	0·472	0·397	0·765	0·855
Yb	0·463	0·453	0·748	0·743	0·808	0·786	0·407	1·29	0·726	0·369	0·418	0·228	0·586	0·277	0·416	0·403	0·705	0·806
Lu	0·0678	0·068	0·105	0·105	0·117	0·113	0·0601	0·19	0·109	0·0522	0·0646	0·0344	0·0825	0·0408	0·0625	0·0571	0·102	0·12
Hf	0·368	0·371	0·871	0·908	0·664	0·657	0·332	1·07	0·657	0·293	0·349	0·198	0·424	0·205	0·347	0·303	0·588	0·592
Ta	0·0538	0·0529	0·0518	0·049	0·0961	0·0785	0·0414	0·137	0·079	0·0354	0·0499	0·0301	0·0616	0·0291	0·0537	0·0434	0·0833	0·0798
Tl	0·00594	0·00619	0·0177	0·0182	0·00649	0·0158	0·00192	0·00331	0·00331	0·00234	0·00661	0·00405	0·0143	0·00528	0·0105	0·0101	–	–
Pb	0·324	0·325	0·236	0·249	0·385	0·274	0·107	0·221	0·165	0·174	0·279	0·588	0·826	0·199	0·583	0·796	0·436	0·562
Th	0·161	0·157	0·103	0·106	0·159	0·120	0·0806	0·248	0·127	0·0569	0·0946	0·0498	0·102	0·0487	0·0881	0·0746	0·139	0·133
U	0·0463	0·0495	0·050	0·111	0·0832	0·0285	0·020	0·116	0·0213	0·0236	0·0539	0·0193	0·0329	0·0221	0·025	0·0336	0·0245	0·0178

(continued)

Table 4: Continued

Formation:	Komati												Hooggenoeg			
Type:	Al-undepleted							Al-depleted					Al-undepleted			Al-depleted
Sample:	SS011	SS011dup	SS012	SS012dup	SS013	SS014	SS015	SS016	SS017	SS018	SS019	SS0110	HOG1	HOG2	HOG3	HOG4
Li	1·35	0·972	1·24	1·30	1·56	1·09	1·2	0·938	1·24	1·93	1·66	2·55	17·8	15·2	13·2	10·2
Sc	11·8	8·61	10·9	10·8	11·2	10·0	10·0	12·7	11·6	13·0	12·0	17·6	38·6	39·0	40·4	22·0
Ti	940	678	835	831	887	771	748	1390	1300	1550	1370	1990	2430	2590	2600	2220
V	81·7	58·4	71·9	74·5	76·3	67·2	65·5	78·2	72·3	79·2	76·7	103	205	224	217	141
Cr	2530	1820	2210	2550	2340	2270	2230	4510	4330	4150	4380	1940	861	905	797	4200
Co	118	85·4	121	120	115	118	124	135	133	129	133	107	57·1	53·1	55·0	127
Ni	2070	1470	2230	2250	2080	2240	2330	1920	1920	1720	1910	1570	164	148	125	2020
Cu	54·3	39·4	40·9	32·1	81·7	46·5	2·72	2·18	10·5	6·05	19·9	41·2	60·7	63·3	72·2	12·8
Zn	64·1	46·4	58·6	63·2	59·4	59·1	57·8	80·3	75·3	77·2	74·8	74·8	64·1	61·7	69·5	74·5
As	–	–	–	0·345	–	–	–	–	–	–	–	–	10·6	1·24	1·25	0·859
Rb	3·03	2·09	2·33	2·28	2·72	3·05	1·26	0·195	0·329	0·124	0·324	2·24	4·74	0·76	0·764	3·48
Sr	29·1	20·7	18·2	17·4	16·7	25·2	12·1	9·87	12·2	10·1	20·4	48·8	90·6	78·9	69·3	12·9
Y	3·24	2·30	2·83	2·71	2·99	2·59	2·54	5·46	5·17	6·06	5·33	8·48	10·3	11·5	10·5	8·23
Zr	7·18	5·02	6·06	6·06	6·47	5·56	5·47	19·7	18·5	22·6	19·6	29·2	21·4	22·5	22·4	22·2
Nb	0·431	0·305	0·374	0·346	0·400	0·331	0·332	1·22	1·15	1·40	1·22	1·72	0·83	0·902	0·895	1·03
Cd	0·0177	0·0129	0·0133	0·0141	0·0157	0·015	0·00968	0·0072	0·0085	0·00897	0·012	0·0237	0·0265	0·0314	0·028	0·0155
Cs	0·487	0·354	0·804	0·852	0·899	1·02	0·47	0·24	0·298	0·25	0·36	0·69	0·145	0·166	0·11	1·90
Ba	11·5	7·94	6·59	6·51	13·5	7·52	3·01	3·37	3·70	3·65	4·08	12·6	238	9·49	14·9	3·96
La	0·523	0·369	0·444	0·447	0·483	0·408	0·398	1·85	1·75	1·96	1·75	2·27	1·08	1·27	1·20	1·31
Ce	1·43	1·01	1·18	1·18	1·28	1·09	1·07	4·48	4·34	4·86	4·43	6·03	2·99	3·50	3·28	3·45
Pr	0·215	0·151	0·18	0·179	0·186	0·166	0·164	0·611	0·616	0·701	0·631	0·906	0·482	0·552	0·526	0·52
Nd	1·06	0·761	0·916	0·902	0·958	0·846	0·82	2·82	2·77	3·14	2·85	4·28	2·58	2·86	2·81	2·56
Sm	0·341	0·241	0·306	0·293	0·329	0·294	0·271	0·778	0·716	0·852	0·771	1·26	0·934	1·01	0·937	0·899
Eu	0·132	0·094	0·116	0·112	0·121	0·107	0·104	0·203	0·223	0·292	0·290	0·416	0·362	0·456	0·414	0·369
Gd	0·477	0·335	0·395	0·388	0·432	0·372	0·362	0·876	0·860	1·01	0·914	1·48	1·33	1·48	1·41	1·28
Tb	0·081	0·0588	0·0709	0·0708	0·0776	0·0661	0·0638	0·153	0·147	0·174	0·153	0·25	0·251	0·267	0·254	0·223
Dy	0·57	0·41	0·47	0·489	0·552	0·454	0·440	0·977	0·938	1·11	0·962	1·59	1·75	1·93	1·80	1·51
Ho	0·124	0·0871	0·108	0·108	0·116	0·0995	0·0963	0·211	0·200	0·235	0·206	0·332	0·382	0·435	0·41	0·315
Er	0·371	0·253	0·316	0·321	0·345	0·299	0·287	0·612	0·569	0·684	0·597	0·932	1·17	1·31	1·24	0·898
Yb	0·363	0·251	0·311	0·313	0·339	0·289	0·277	0·568	0·538	0·646	0·556	0·863	1·17	1·31	1·24	0·796
Lu	0·0535	0·0378	0·0468	0·0474	0·0511	0·0432	0·0428	0·0856	0·0795	0·094	0·0849	0·131	0·175	0·194	0·186	0·114
Hf	0·213	0·142	0·172	0·183	0·185	0·158	0·156	0·520	0·496	0·602	0·522	0·809	0·629	0·672	0·681	0·638
Ta	0·028	0·0198	0·0239	0·0216	0·0253	0·0228	0·0213	0·0833	0·0756	0·094	0·0812	0·112	0·0524	0·0589	0·0613	0·0677
Tl	0·0211	0·0156	0·0194	0·0154	0·0234	0·0224	0·013	0·00231	0·0024	0·00168	0·00228	0·0241	0·0496	0·00579	0·00744	0·138
Pb	0·184	0·129	0·165	0·102	0·164	0·262	0·144	0·291	0·296	0·334	0·388	0·388	0·260	0·323	0·242	0·841
Th	0·0354	0·0251	0·0284	0·0273	0·0312	0·0274	0·0278	0·186	0·173	0·212	0·184	0·215	0·0811	0·0882	0·0876	0·117
U	0·0112	0·00744	0·00899	0·00888	0·00807	0·00833	0·00839	0·0416	0·0414	0·046	0·0442	0·0476	0·0202	0·0235	0·0211	0·0275

Table 4: Continued

Formation:	Hooggenoeg Al-depleted			Weltevreden Al-enriched										
Sample:	HOG5	HOG6	HOG6dup	MC6-1	MC6-4	MC6-4dup	MC7-6	MC5-1	MC5-1	MC5-1	MC5-1	MC5-3	MC5-5	MC5-6
Li	6·52	15·4	16·3	18·4	4·23	4·23	9·97	1·82	1·86	1·82	1·77	2·98	47·8	17·3
Sc	16·9	25·1	23·5	34·3	12·5	12·4	19·8	7·89	10·1	7·86	8·06	5·71	32·7	38·2
Ti	1440	2610	2540	1670	530	536	953	264	342	262	276	504	1480	2380
V	109	166	163	145	61·5	62·3	108	31·0	41·0	30·6	30·4	65·9	158	241
Cr	6480	3770	3740	2370	3180	3220	2860	2070	2690	2020	1950	6490	3800	422
Co	147	117	113	75·1	114	115	103	117	161	116	121	165	105	46·4
Ni	2580	1730	1780	713	1910	1940	1560	2730	3810	2720	2790	2760	1280	189
Cu	49·6	100	101	33·9	26·0	26·4	20·3	10·2	13·9	10·0	10·3	8·48	7·92	6·19
Zn	70·5	67·5	67·2	53·3	49·1	50·3	58·9	37·2	52·4	37·2	40·6	86·9	51·5	35·4
As	1·35	3·23	3·00	–	0·561	0·609	–	–	–	–	1·64	–	–	–
Rb	1·13	1·21	1·30	4·38	0·162	0·216	3·00	0·165	0·260	0·182	0·199	0·238	0·979	0·448
Sr	8·32	14·3	14·1	5·59	6·22	6·23	6·98	3·10	4·06	3·12	3·43	3·78	4·90	11·4
Y	5·19	9·40	9·33	13·9	2·48	2·54	4·36	1·23	1·61	1·22	1·26	1·98	6·55	11·1
Zr	12·6	24·0	24·2	43·1	4·51	4·50	6·98	2·09	2·92	2·16	2·10	3·23	11·8	19·3
Nb	0·582	1·17	1·13	2·83	0·143	0·149	0·339	0·0698	0·0857	0·0747	0·0652	0·127	0·502	0·667
Cd	0·015	0·0383	0·0462	–	0·00757	0·00788	–	–	–	–	0·0092	–	–	–
Cs	0·756	0·875	0·934	2·05	0·133	0·135	1·48	0·0685	0·072	0·0715	0·0735	0·153	0·832	0·414
Ba	8·53	3·06	3·09	5·04	0·586	0·545	2·50	0·398	0·333	0·394	14·6	0·395	11·5	4·66
La	0·746	1·37	1·37	7·66	0·195	0·188	0·269	0·0968	0·0956	0·0946	0·101	0·141	0·469	0·661
Ce	1·90	3·62	3·73	15·5	0·540	0·509	0·797	0·275	0·271	0·271	0·281	0·395	1·38	2·09
Pr	0·291	0·562	0·562	1·78	0·085	0·0847	0·137	0·0448	0·0477	0·0446	0·0463	0·0652	0·231	0·365
Nd	1·41	2·81	2·72	6·70	0·455	0·452	0·75	0·244	0·245	0·238	0·236	0·348	1·24	2·05
Sm	0·525	1·01	0·964	1·38	0·189	0·169	0·292	0·0922	0·0916	0·0833	0·0894	0·126	0·446	0·77
Eu	0·229	0·328	0·327	0·307	0·0674	0·0793	0·129	0·0433	0·0393	0·0422	0·0472	0·056	0·199	0·247
Gd	0·775	1·48	1·50	1·70	0·283	0·281	0·497	0·145	0·142	0·140	0·137	0·199	0·741	1·31
Tb	0·138	0·263	0·261	0·296	0·0546	0·0572	0·0916	0·0272	0·026	0·0265	0·0278	0·0375	0·128	0·239
Dy	0·968	1·81	1·76	2·10	0·380	0·421	0·679	0·198	0·184	0·188	0·208	0·267	0·972	1·76
Ho	0·194	0·364	0·369	0·491	0·0917	0·091	0·155	0·045	0·0448	0·0416	0·0446	0·0624	0·227	0·401
Er	0·562	1·02	0·993	1·59	0·296	0·292	0·483	0·138	0·140	0·135	0·146	0·192	0·688	1·23
Yb	0·493	0·888	0·863	1·71	0·285	0·299	0·492	0·150	0·150	0·153	0·150	0·209	0·740	1·25
Lu	0·0747	0·126	0·125	0·263	0·0448	0·0456	0·0754	0·0233	0·0237	0·0239	0·0221	0·0330	0·112	0·190
Hf	0·377	0·713	0·725	1·19	0·138	0·132	0·212	0·0673	0·0685	0·0647	0·0659	0·0867	0·343	0·592
Ta	0·0377	0·0737	0·0736	0·14	0·011	0·00928	0·0156	0·00487	0·00352	0·00425	0·00408	0·0147	0·0235	0·0421
Tl	0·0191	0·166	0·136	–	0·0028	0·00466	–	–	–	–	0·00197	–	–	–
Pb	0·638	0·736	0·777	0·699	0·044	0·0345	4·18	0·0458	0·0304	0·0320	<DL	0·0568	0·159	1·19
Th	0·0648	0·121	0·117	1·42	0·0104	0·0134	0·0194	0·00668	0·0076	0·00831	0·00612	0·00893	0·0357	0·0499
U	0·0166	0·0328	0·0306	0·323	0·0045	0·00595	0·00682	0·00354	0·00363	0·00375	0·0038	0·00381	0·00858	0·0153

(continued)

Table 4: Continued

| Formation: | Weltevreden | | | | | | | | | | | | | |
| Type: | Al-enriched | | | | | Al-depleted | Al-undepleted | | | Al-enriched | | | | |
Sample:	MC5-7	MC5-7	MC4-3	MC4-3dup	MC4-4	SA700-1	SA719-1	SA719-2	SA719-4	WP101	WP101dup	WP101dup	WP102	WP102dup
Li	10·1	10·0	8·76	8·78	5·21	8·94	4·96	4·67	4·78	2·46	2·52	2·55	1·36	1·38
Sc	21·1	22·0	15·1	15·1	12·9	17·8	15·4	27·8	12·6	8·30	8·63	7·98	8·53	8·62
Ti	1100	1110	594	602	478	1670	914	2180	711	251	249	245	267	285
V	115	119	76·3	77·2	61·4	97·8	81·1	175	62·0	34·2	35·4	34·3	36·2	36·3
Cr	2920	3060	5250	5160	4120	2520	2480	2170	2260	2300	2370	2330	1880	1940
Co	86·1	89·8	149	151	136	85·6	126	83·3	143	146	150	150	123	119
Ni	1440	1540	1570	1580	2620	2540	2550	608	2760	2330	2410	2480	2780	2760
Cu	104	112	20·6	20·8	11·9	586	12·7	139	5·01	2·05	2·08	2·30	2·22	1·94
Zn	42·6	45·3	56·5	57·4	55·2	78·0	50·8	61·2	56·6	46·6	46·8	47·8	30·6	30·4
As	–	–	–	–	–	–	–	–	–	0·376	0·294	0·368	0·579	0·463
Rb	0·857	0·935	1·19	1·21	0·776	0·754	2·15	1·15	2·12	0·178	0·203	0·172	0·0253	0·0265
Sr	7·16	7·44	1·04	1·06	2·58	5·65	2·72	9·74	4·70	2·40	2·49	2·33	1·17	1·14
Y	4·66	4·88	2·67	2·68	2·20	12·2	4·00	7·91	3·24	1·15	1·15	1·13	1·22	1·22
Zr	8·64	9·24	5·37	5·46	3·84	17·2	9·20	20·8	6·77	1·94	1·99	2·01	2·16	2·29
Nb	0·305	0·359	0·165	0·197	0·144	0·909	0·390	1·07	0·301	0·0642	0·0653	0·0585	0·0746	0·0788
Cd	–	–	–	–	–	–	–	–	–	0·00638	0·00578	0·00548	0·0147	0·00848
Cs	0·642	0·674	0·225	0·23	0·103	0·690	0·522	0·666	2·35	0·384	0·392	0·429	0·00392	0·0031
Ba	11·2	11·5	0·445	0·574	0·573	9·24	1·85	2·45	11·9	0·943	0·971	0·900	0·226	0·250
La	0·33	0·331	0·197	0·192	0·158	3·20	0·443	0·917	0·407	0·0726	0·0713	0·0708	0·112	0·101
Ce	1·07	1·05	0·557	0·571	0·445	3·45	1·21	2·64	1·09	0·199	0·201	0·209	0·270	0·286
Pr	0·18	0·183	0·0956	0·0939	0·0734	0·856	0·193	0·424	0·174	0·034	0·0338	0·0345	0·0448	0·044
Nd	0·982	0·967	0·505	0·474	0·369	3·99	0·963	2·19	0·899	0·206	0·201	0·187	0·235	0·235
Sm	0·359	0·367	0·176	0·174	0·141	1·08	0·345	0·744	0·310	0·0744	0·0757	0·0795	0·0824	0·0892
Eu	0·134	0·135	0·0754	0·076	0·0584	0·239	0·126	0·27	0·136	0·0387	0·0356	0·0311	0·0526	0·0514
Gd	0·567	0·570	0·283	0·285	0·225	1·47	0·487	1·070	0·420	0·132	0·124	0·122	0·134	0·138
Tb	0·106	0·0981	0·0483	0·0492	0·042	0·223	0·0848	0·180	0·0705	0·0216	0·0245	0·0229	0·0273	0·0267
Dy	0·74	0·756	0·396	0·379	0·306	1·41	0·557	1·29	0·492	0·182	0·195	0·177	0·199	0·208
Ho	0·166	0·166	0·0879	0·0843	0·0707	0·296	0·128	0·281	0·110	0·0392	0·0425	0·0418	0·0454	0·0473
Er	0·509	0·509	0·264	0·266	0·213	0·798	0·382	0·842	0·334	0·128	0·131	0·131	0·135	0·146
Yb	0·523	0·531	0·277	0·283	0·229	0·645	0·379	0·860	0·333	0·142	0·142	0·141	0·150	0·146
Lu	0·0788	0·0811	0·042	0·0429	0·0344	0·0971	0·0583	0·131	0·0503	0·0229	0·0219	0·0225	0·0243	0·0245
Hf	0·255	0·263	0·136	0·144	0·102	0·436	0·235	0·577	0·185	0·0614	0·0613	0·0618	0·0671	0·0672
Ta	0·019	0·0168	0·00734	0·00825	0·00586	0·0433	0·0173	0·0493	0·0156	0·0048	0·00357	0·00343	0·0037	0·00389
Tl	–	–	–	–	–	–	–	–	–	0·0018	0·00224	0·0012	0·00227	0·00158
Pb	0·0926	0·109	0·0914	0·0847	0·0874	0·225	0·525	0·771	1·54	0·0567	0·0567	0·0031	0·141	0·00574
Th	0·0268	0·0245	0·0138	0·0139	0·0112	0·120	0·0467	0·107	0·0401	0·00471	0·0045	0·00458	0·0057	0·00757
U	0·00753	0·00891	0·00516	0·00569	0·00544	0·0418	0·0145	0·0411	0·0122	0·00243	0·00371	0·00289	0·00337	0·00399

(continued)

Table 4: Continued

| Formation: | Weltevreden | | | | | | | |
| Type: | Al-enriched | | | | | | | |
Sample:	WP103	WP104	WP105	WP105dup	WP106	WP107	WP108	WP109
Li	12·6	14·8	15·2	15·1	16·5	58·5	16·5	5·79
Sc	25·1	17·0	17·1	17·6	40·2	20·6	37·8	13·3
Ti	1890	724	656	675	2910	866	2340	542
V	187	81·3	79·6	78·1	292	104	235	60·7
Cr	1200	2420	3780	3790	39·9	2840	416	2880
Co	34·8	106	96·9	101	46·1	99·0	44·4	117
Ni	374	1850	1360	1390	87·3	1630	178	1940
Cu	15·0	56·8	5·69	6·77	7·75	25·8	6·64	25·4
Zn	35·0	48·9	57·5	59·0	47·9	75·9	36·2	54·7
As	0·612	0·311	0·380	0·334	0·509	0·283	0·514	0·322
Rb	0·135	1·94	0·403	0·322	1·39	0·689	0·343	1·53
Sr	5·51	3·08	2·89	3·01	69·3	45·1	13·3	30·8
Y	9·03	3·28	3·35	3·35	13·9	4·25	9·95	2·43
Zr	17·2	5·83	5·03	5·26	26·3	7·17	17·3	4·32
Nb	0·575	0·179	0·170	0·174	0·866	0·206	0·564	0·134
Cd	0·0139	0·0109	0·00614	0·00581	0·0138	0·0101	0·0126	0·00732
Cs	0·0915	1·28	0·476	0·446	0·416	0·927	0·164	0·109
Ba	3·00	2·80	4·56	4·53	42·1	6·24	9·95	1·74
La	0·689	0·234	0·407	0·399	1·06	0·279	0·727	0·181
Ce	2·04	0·674	0·875	0·823	3·17	0·807	2·15	0·511
Pr	0·333	0·111	0·134	0·130	0·535	0·140	0·364	0·0808
Nd	1·79	0·584	0·687	0·629	2·77	0·759	1·90	0·422
Sm	0·665	0·230	0·234	0·235	1·08	0·29	0·707	0·192
Eu	0·298	0·118	0·0942	0·0971	0·397	0·111	0·297	0·073
Gd	1·03	0·369	0·380	0·383	1·59	0·478	1·21	0·295
Tb	0·200	0·0709	0·0682	0·0697	0·297	0·0936	0·227	0·0551
Dy	1·36	0·539	0·500	0·511	2·21	0·679	1·64	0·389
Ho	0·329	0·124	0·118	0·123	0·499	0·163	0·376	0·0915
Er	0·954	0·394	0·390	0·374	1·53	0·495	1·15	0·278
Yb	0·951	0·398	0·386	0·378	1·54	0·521	1·18	0·290
Lu	0·141	0·0622	0·0596	0·0615	0·235	0·0786	0·177	0·0433
Hf	0·482	0·178	0·162	0·157	0·762	0·232	0·543	0·135
Ta	0·0355	0·0113	0·0102	0·0111	0·054	0·0151	0·0381	0·00799
Tl	0·00248	0·00129	0·00307	0·00295	0·00531	0·00252	0·00231	0·00438
Pb	<DL	0·390	1·68	1·62	0·136	0·536	0·226	<DL
Th	0·0542	0·0140	0·0202	0·0204	0·0769	0·0186	0·0478	0·0108
U	0·0161	0·00396	0·011	0·0105	0·0222	0·00596	0·0159	0·00454

dup, duplicate; —, not determined; <DL, below detection limit.
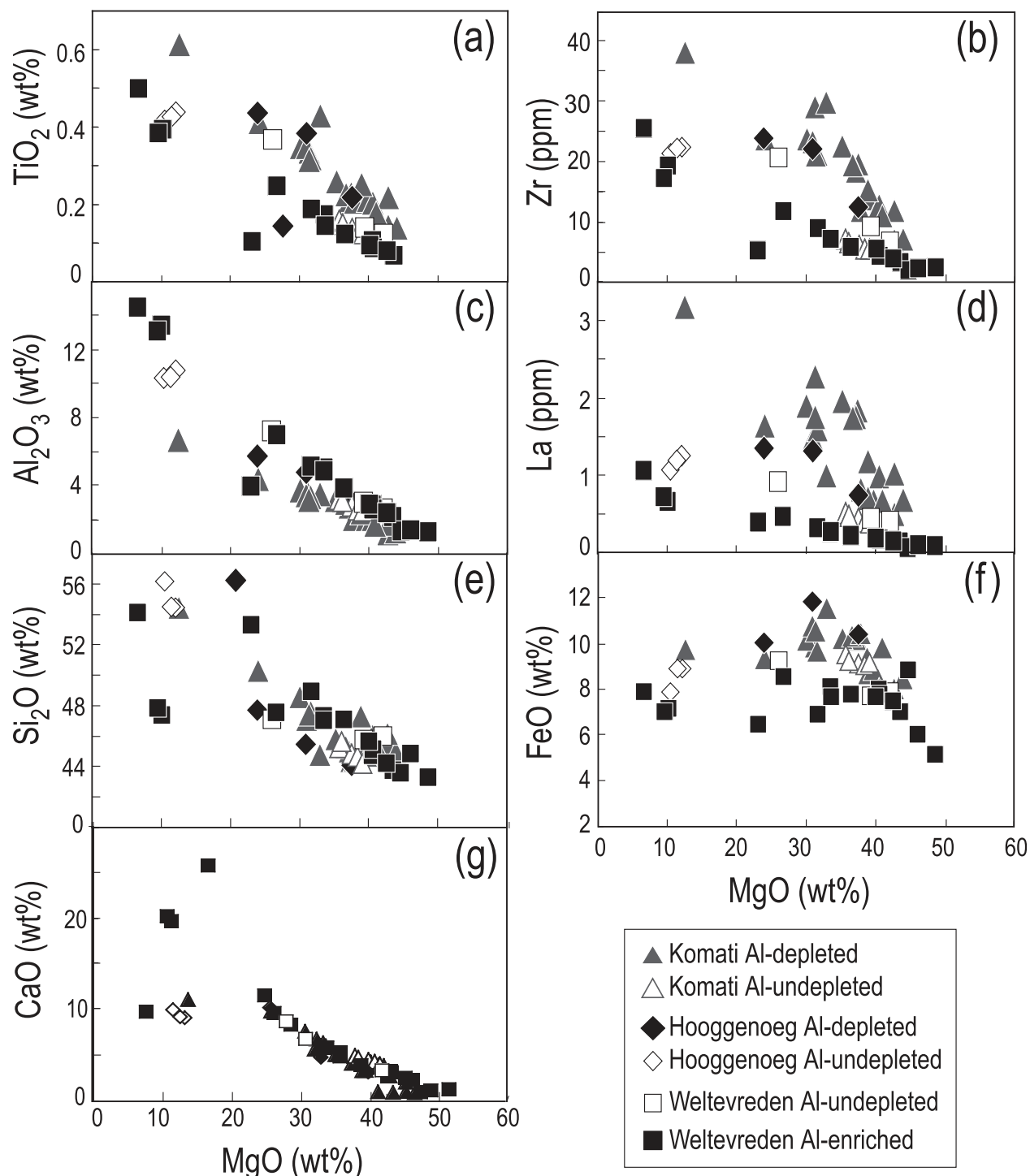
Fig. 4. Selected bulk-rock major elements, Zr and La vs MgO for all analyzed samples. Major-element concentrations (wt %) and Zr and La concentrations (ppm) are normalized to 100% on a volatile-free basis. (See Electronic Appendix 3 for FeO calculation method.)

extent of MgO mobility was minor [see detailed arguments by Arndt *et al.* (2008)]. Confirmation can be found by comparing the whole-rock composition constructed from the modal mineralogy and mineral compositions. For example,

the spinifex-textured komatiite BD5 from the Komati Formation contains about 50 ± 5 modal % olivine (Arndt, 1986). The olivine, which has the composition Fo_{90-94} and contains 49–51% MgO, would have contributed about
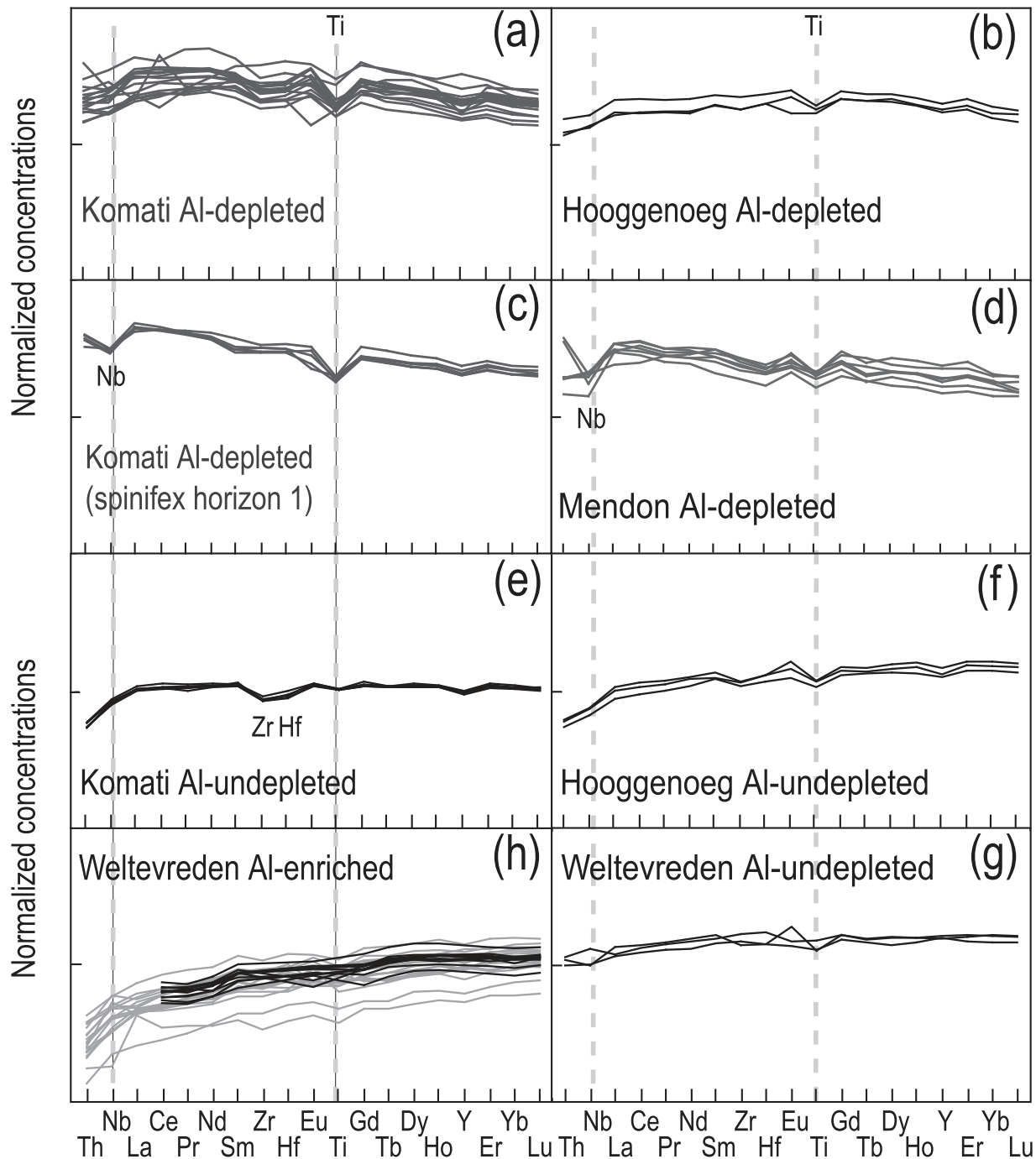
Fig. 5. Selected trace-element spectra. Concentrations are normalized to 100% on a volatile-free basis and to the primitive mantle values of McDonough & Sun (1995). They are also normalized to the parental magma MgO content (Electronic Appendix 3). Mendon Al-depleted komatiite spectra are from Lahaye *et al.* (1995). In (h), grey spectra are data from this study and black spectra are from Kareem (2005).

$0{\cdot}50 \times 50 = 25$ wt % MgO to the rock composition. The clinopyroxene (25 modal %; 10–20 wt % MgO) and interstitial glass (25 modal %; 6–10 wt %) in the matrix contribute another 5 wt %, to bring the total to 30 wt % MgO. This value is very similar to the MgO content in the whole-rock, which is 30·6% MgO.

Significant olivine accumulation can be ruled out, and the lack of significant MgO mobility is confirmed when the textures of the rocks are taken into account. Samples from chilled margins, from random spinifex lava or fine-grained tuff are unlikely to contain significant excess olivine and their MgO contents broadly coincide with
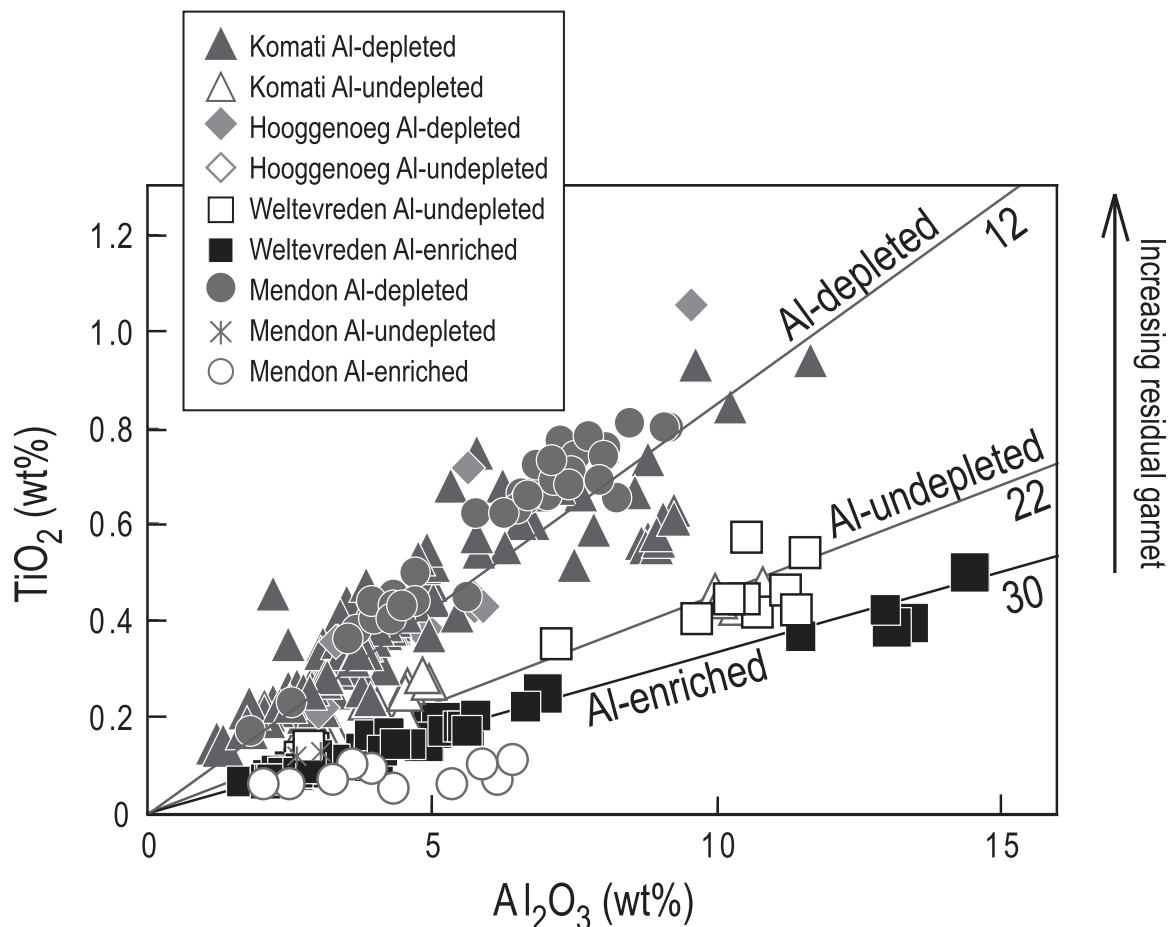
Fig. 6. TiO_2 vs Al_2O_3 diagram for Barberton komatiites. Data are normalized to 100% on a volatile-free basis. Larger symbols are data from this study and smaller symbols are data from the literature: Viljoen & Viljoen (1969), Williams & Furnell (1979), Smith *et al.* (1980), Smith & Erlank (1982), Viljoen *et al.* (1983), Lahaye *et al.* (1995), Byerly (1999), Parman *et al.* (2003), Kareem (2005) and Cooper (2008). Numerical values on the best-fit trends are Al_2O_3/TiO_2 ratios.

those estimated for the komatiite liquids. Notable examples include the random spinifex lavas of the Komati Formation [our analyses and those of Parman *et al.* (2003)] and the tuffs of the Mendon Formation [our analyses and those of Steigler et al. (2008, 2010)]. On the basis of arguments such as these we are convinced that MgO was relatively immobile in most samples and that measured values are close to those of the unaltered volcanic rocks.

Parental magma compositions

Major-element compositions and minimum eruption temperatures for the parental magmas were estimated using the method presented in Supplementary Data Electronic Appendix 3. For each formation we used the intercepts of olivine control lines to estimate the average composition of the olivine that accumulated in the flows. The MgO content of this olivine was taken as a minimum value for the liquidus olivine. When possible, this composition was compared with that of fresh olivine analyzed by electron

microprobe. Then, using an Mg–Fe olivine–melt partition coefficient of 0·35 (Matzen *et al.*, 2011), we estimated the liquid composition. As illustrated in Fig. 9, we calculate the FeO/MgO of a liquid in equilibrium with the most magnesian olivine, then use the intercept between the line representing the liquid FeO/MgO ratio and the whole-rock compositions to estimate the MgO content of the parental liquid. Most of the uncertainty on the liquid composition comes from the variation of FeO that was used to calculate the parental liquid concentrations of the other major elements. Minimum eruption temperatures were estimated using the methods of Nisbet (1982) and Herzberg & Asimow (2008).

Three intercepts were calculated from TiO_2, Al_2O_3 and Zr data for Al-depleted komatiites from the Komati Formation. They yield a Mg# of ~93·5% for the olivine, which (considering the uncertainty) is consistent with the maximum Mg# we measured on fresh olivine kernels by electron microprobe (92·3%) and with those previously
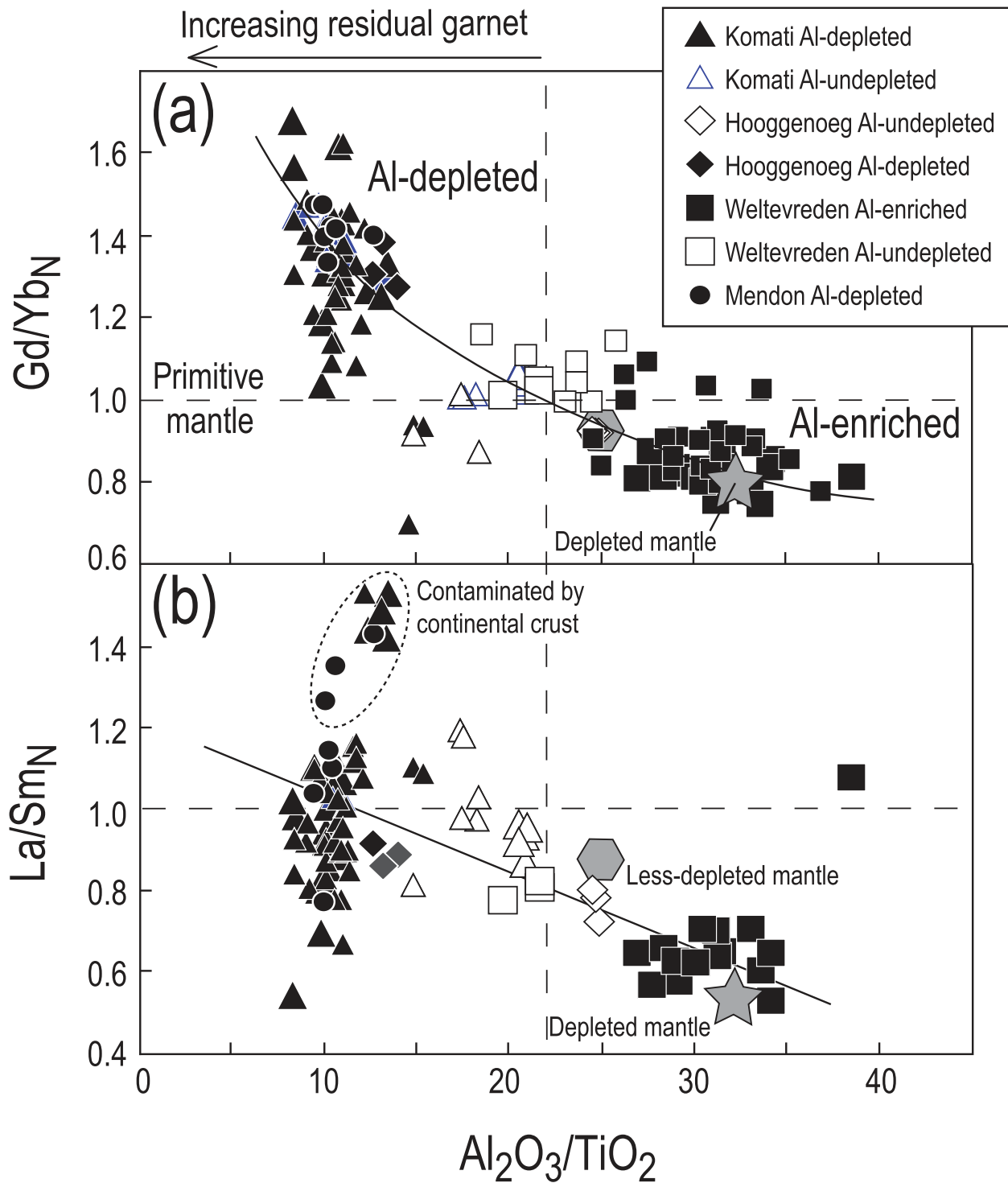
Fig. 7. Gd/Yb_N (a) and La/Sm_N (b) vs Al_2O_3/TiO_2 diagram for Barberton komatiites. La, Sm, Gd and Yb concentrations are normalized to the parental magma MgO content and to the primitive mantle values of McDonough & Sun (1995). Larger symbols are data from this study and smaller symbols are data from the literature: Viljoen & Viljoen (1969), Williams & Furnell (1979), Smith *et al.* (1980), Smith & Erlank (1982), Viljoen *et al.* (1983), Lahaye *et al.* (1995), Parman *et al.* (2003), Kareem (2005) and Cooper (2008).

Table 5: Composition (in wt %) of the olivine measured with highest Mg# in each sample

	Mg#	SiO$_2$	TiO$_2$	Al$_2$O$_3$	FeO	MnO	MgO	CaO	NiO	CoO	Cr$_2$O$_3$	MnO/FeO	NiO × FeO/MgO	Total
BD6	89·36	40·55	0·005	0·02	10·29	0·17	48·48	0·23	0·36	0·02	0·10	0·016	0·08	100·22
BD12	92·33	40·68	0·006	0·04	7·42	0·12	50·09	0·24	0·44	0·02	0·17	0·017	0·06	99·22
SA719-1	93·68	40·77	0·005	0·06	6·15	0·10	51·12	0·17	0·43	0·01	0·21	0·016	0·05	99·02
MC6-4	92·51	41·31	0·005	0·05	7·37	0·12	51·09	0·16	0·38	0·02	0·14	0·016	0·05	100·64
WP109	92·53	40·71	0·005	0·05	7·31	0·12	50·75	0·15	0·37	0·02	0·16	0·016	0·05	99·64
MC4-2	93·14	40·79	0·004	0·06	6·71	0·11	51·06	0·13	0·41	0·02	0·24	0·016	0·05	99·52
MC4-4	93·11	40·58	0·003	0·04	6·68	0·10	50·63	0·13	0·40	0·01	0·23	0·015	0·05	98·81
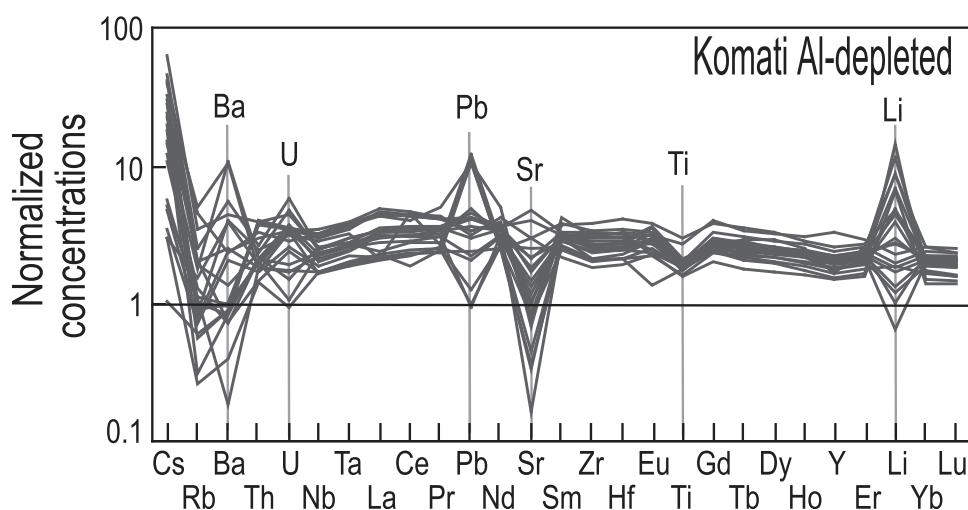
Fig. 8. Trace-element spectra for Komati Al-depleted komatiites including mobile elements. Concentrations are normalized as in Fig. 5.

measured by Parman *et al.* (1997) (93%). Using the intercept value, we calculated that the parental magma contained 26% MgO (Fig. 9a), which is close to the average MgO of 27% of the chilled margins analyzed by Viljoen *et al.* (1983) and Parman *et al.* (2004). This MgO corresponds to an eruption temperature of ∼1550°C.

Data from Al-undepleted komatiites of the Komati Formation are too sparse to provide reliable olivine differentiation lines and MgO intercepts. Instead, we used the compositions of chilled margins from Parman *et al.* (2004; plotted in Fig. 9b) to estimate the composition of the parental magma. Our estimate is MgO$_{liquid}$ ∼30%, which corresponds to an eruption temperature of ∼1600°C.

For Al-enriched komatiites of the Weltevreden Formation in the Pioneer Complex, four intercepts were calculated using TiO$_2$, Al$_2$O$_3$, Zr and La data. They yield a Mg# of ∼93%, which is similar to the maximum Mg# that we measured by electron microprobe (93·1%) and to that measured by Cooper (2008) (92·9%). From this value, we

calculated ∼20% MgO in the liquid (Fig. 9c). Other observations suggest, however, that the parental liquids of Al-enriched komatiites from the Pioneer Complex had a higher MgO content. The fine-grained tuffs interlayered with the sills (plotted in Fig. 9c) should have a composition close to that of their parental liquid. Even though these samples plot on the same olivine control lines as other samples from the Pioneer Complex, they are far more magnesian, with an average MgO content of ∼33% [our data and data from Stiegler *et al.* (2010)]. Moreover, the komatiites from other parts of the Weltevreden Formation studied by Kareem (2005) have similar trace-element spectra (Fig. 5) to those of the Pioneer Complex and seem to come from similar parental liquids; they also plot on the same olivine control lines (Fig. 9c and Electronic Appendix 3). Using the extremely magnesian olivine containing up to 95·6% Fo measured by Kareem (2005), we estimated a MgO content of about 30% in the parental liquid (Fig. 9c). From the compositions of glass inclusions
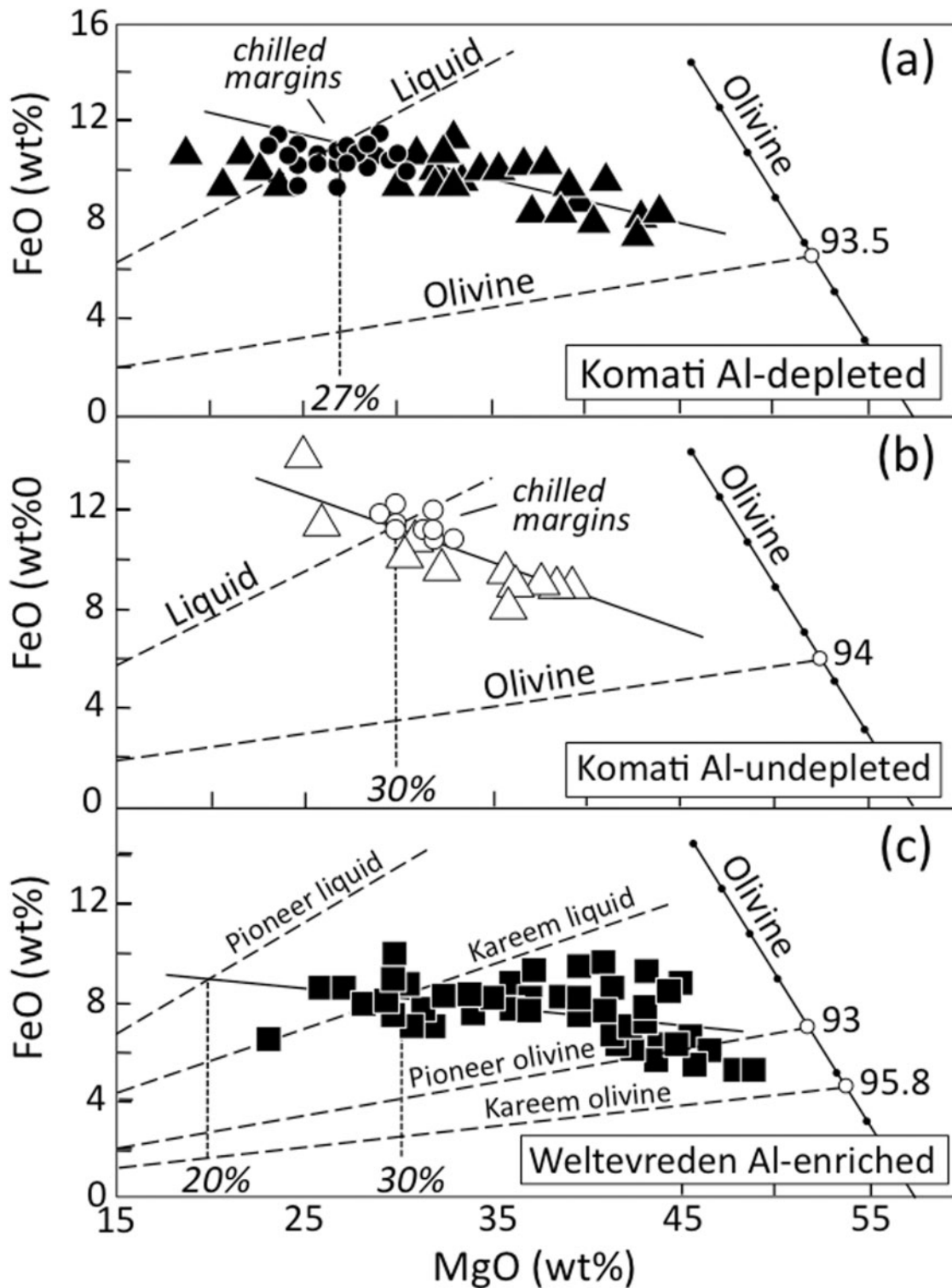
Fig. 9. FeO vs MgO variation diagrams. Concentrations (wt %) are normalized to 100% on a volatile-free basis and the method used to calculate FeO concentrations is given in Electronic Appendix 3. Continuous lines are least-square regressions that approximate olivine differentiation trends. Sloping lines with dots represents the composition of olivine. The dashed line labeled 'Olivine' represents the FeO/MgO ratio of the most magnesium analysed olivine, and dashed lines labeled 'Liquid' represent the FeO/MgO ratio of the liquids in equilibrium with these olivines. The MgO values in italics are the estimated liquid MgO contents. Literature data are from Viljoen & Viljoen (1969), Williams & Furnell (1979), Smith *et al.* (1980), Smith & Erlank (1982), Viljoen *et al.* (1983), Lahaye *et al.* (1995), Parman *et al.* (2003), Kareem (2005) and Cooper (2008).

in these olivines, Thompson *et al.* (2003) proposed that the parental liquid contained 34·8% MgO; and Connolly *et al.* (2012) have recorded 30·9% MgO in a chilled margin sample from Kareem's collection.

These arguments provide permissive evidence that all three types of rock in the Weltevreden Formation—the Pioneer Complex komatiites, the ultramafic tuffs, and the komatiites from Kareem's study area—are comagmatic and related to one another by fractional crystallization of an ∼33% MgO parental liquid, which is represented by the tuffs. The crystallization could have occurred as the magma rose through the crust, or at shallower levels within sills or flows. Simulations using Danyushevsky's (2001) Petrolog program indicate that about 40% olivine crystallization is required to produce the relatively evolved komatiites of the Pioneer Complex from a 33% MgO liquid. The MgO content of the parental liquid corresponds to an eruption temperature of ∼1650°C.

There are too few data from this study and from the literature to calculate reliable olivine control lines and olivine Mg# for the Hooggenoeg komatiites and for Al-undepleted komatiites from the Weltevreden Formation. For these we assumed 30% MgO for the parental liquid with Mg# ∼94% for the olivine, a value close to the maximum Mg# = 93·7% that we measured in Al-undepleted komatiites from the Weltevreden Formation (Table 5).

Calculated parental magma and liquidus olivine compositions, together with eruption temperatures, are summarized in Table 6.

Petrogenesis of the Barberton komatiites

Source compositions

Sobolev *et al.* (2007) developed a method, based on the analysis of olivine primocrysts in mantle-derived magmas, to evaluate the proportions of peridotite and pyroxenite (recycled oceanic crust) in the source of mafic magmas. Olivines from the Barberton komatiites have high MnO/FeO (0·015–0·018) and low Ni*Fe/Mg (0·05–0·08) ratios [Table 5 and Sobolev *et al.* (in preparation)], which, according to Sobolev *et al.* (2007), correspond to a low proportion of pyroxenite. On this basis, we can assume that their source was essentially normal peridotite.

Almost all Barberton komatiites are LREE depleted (Fig. 7b) and have positive initial ε_{Nd} and ε_{Hf} (Gruau *et al.*, 1990; Lahaye *et al.*, 1995; Blichert-Toft & Arndt, 1999; Chavagnac, 2004; Robin-Popieul *et al.*, in preparation). These values indicate that their mantle sources were moderately depleted in incompatible trace elements. However, the La/Sm$_N$ ratios are relatively high (in most cases above 0·8, compared with ∼0·67 in N-MORB), indicating that their mantle sources were less depleted than modern depleted mantle. This is consistent with previous estimates of the degree of depletion of Archean komatiite sources from the Sm–Nd and Lu–Hf systematics of well-characterized Archean komatiites (Blichert-Toft & Puchtel, 2010).

Conditions of melting

The low concentrations of TiO_2 (<0·5%) and incompatible trace elements (∼0·3–3 times primitive mantle) in the parental liquids suggest that the degree of melting (F) was high; for example, if we assume batch melting and partition coefficients of zero for highly incompatible elements, we estimate that F would be between 0·3 and 0·5 (30–50% melting). In practice, these values are only indicative because they do not take into account any initial depletion of the source nor complications introduced by more complex melting mechanisms, but they show clearly that these komatiites did not form as near-solidus melts.

As illustrated by the phase diagram reproduced as Fig. 10a and b, the high MgO contents (∼30%) in the calculated parental liquids require that the komatiite magmas formed either by a high degree of partial melting (>50%) or by melting at high pressure (>15 GPa; Green, 1975; Herzberg, 1992). The rationale behind this statement is as follows: the most magnesian mineral in the mantle is olivine and only when this mineral extensively melts does the liquid reach high MgO contents. Olivine is the liquidus mineral of mantle peridotite only at low and moderate P (Fig. 10b; Zhang & Herzberg, 1994), but as P increases it becomes increasingly fusible compared with the other minerals, and at about 14 GPa it is replaced at the liquidus by garnet. Therefore, for olivine to extensively melt so as to produce liquid with a high MgO content, either F or P, or both, must be high (Herzberg, 1995).

Using data from McKenzie & Bickle (1988), Richter (1988), Herzberg & Zhang (1996) and Herzberg & O'Hara (2002), we can assume that the adiabatic temperature gradient along the ascent path was −0·4°C km^{-1} for the solid source, −1·4°C km^{-1} for the partially molten source, and −1°C km^{-1} for the liquid. Tracing an adiabatic liquid ascent path from the eruption temperature at the surface to the point at which it intersects the solidus gives the minimum depth of melting. If we accept that the Barberton komatiitic magmas were anhydrous and erupted at about 1600°C, Fig. 10a shows that the source crossed the solidus at a pressure of ∼5 GPa, corresponding to a depth of about 150 km. The composition of the melt produced at this depth differs, however, from that of the Barberton komatiites in three important respects; (1) the MgO content of near-solidus melts at 5 GPa is only around 22 wt % (Fig. 10b), far less than that estimated for the parental komatiite liquids; (2) the low trace-element contents of the komatiites indicate that they are not near-solidus melts, as is the case for the liquid produced at 5 GPa; (3) Al-depleted komatiites—those typical of the Barberton belt—form in the field of garnet stability, which, when the degree of melting is high, lies at pressures greater than 10 GPa (Green, 1975; Ohtani *et al.*, 1989;

Table 6: Estimated parental magma compositions

	Komati Al-depleted	Komati Al-undepleted	Weltevreden Al-enriched
SiO_2	48 ± 1	46 ± 0.5	48 ± 1
TiO_2	0.4 ± 0.05	0.2 ± 0.025	0.2 ± 0.05
Al_2O_3	4 ± 0.5	3.5 ± 0.5	5 ± 1
FeO	11 ± 0.5	12 ± 1	8 ± 1
MgO	27 ± 3	30 ± 2	33 ± 2
CaO	8 ± 1.5	6 ± 1	5 ± 2
Al_2O_3/TiO_2	10	18	25
Estimated Mg# of the first olivine crystallizing	0.935	0.94	0.956
Minimum eruption temperature (°C)	1550 ± 60	1600 ± 40	1650 ± 40

Concentrations in weight per cent. We considered that the volatile content is negligible.

Zhang & Herzberg, 1994). In view of these constraints, it is probable that at least the Al-depleted komatiites formed in the shaded region in Fig. 10b. If melt escaped directly to the surface from this depth, it would erupt at a temperature greater than 1700°C, well above its 1 atm liquidus. There is little field or petrological evidence that komatiites were superheated when they erupted, and it is therefore probable that the melt lost heat to its surroundings during its ascent. A possible ascent path of the komatiite parental magma is shown in Fig. 10a.

Comparison of the melting conditions for the different komatiite types

From the chemical characteristics of the parental magmas, we can infer that the degree of melting was higher and the pressure of melting lower for Al-undepleted and Al-enriched komatiites than for Al-depleted komatiites. Only the latter have low Al_2O_3 contents and depleted HREE (Fig. 7), features attributed to the retention of garnet in the residue and to melting at high pressure. The parental magmas of the Al-depleted komatiites also have higher FeO contents than the parental magma of the Al-enriched komatiites (Fig. 4f), which provides additional evidence for high *P* and/or low *F* (Walter, 1998; Herzberg, 2004).

The Al-undepleted and Al-enriched komatiites show variable degrees of depletion of the more incompatible elements, a feature generally attributed to extraction of melt from the source that subsequently yielded the komatiites. Radiogenic isotope studies of komatiites from Barberton (e.g. Blichert-Toft & Arndt, 1999; Blichert-Toft & Puchtel, 2010) and elsewhere reveal no systematic differences between the isotopic compositions of the various types of komatiite, suggesting that the depletion event immediately preceded the melting event. Arguments such as these have led to the hypothesis that these types of komatiite formed by fractional melting; that is, a process whereby melt is continuously extracted producing an ever more refractory source, or 'critical melting', a term that refers to a variant of fractional melting during which a proportion of melt is retained in the source (Maaløe, 1982). As explained below, we will argue that the features of Al-undepleted and Al-enriched komatiites can be explained by critical melting under conditions in which a large proportion of melt remains in the source.

A new melting model for the Barberton komatiites

Melting mechanism

For the Barberton komatiites, fusion of the mantle source started very deep, either at the base of upper mantle or even in the lower mantle (Miller *et al.*, 1991; Herzberg, 1995). High-pressure compressibility experiments (Rigden *et al.*, 1988; Agee, 1998; Suzuki & Ohtani, 1998; Sakamaki *et al.* 2010) have shown that at pressures corresponding to those in the lower part of the upper mantle, between 10 and 15 GPa, the density of komatiite melt is similar to that of solid peridotite. In the case of melting at low pressure (the conditions that produce basaltic magma), the liquid is far less dense that the solid and it escapes as soon as the degree of melting (and the porosity) exceeds 1–2% (Langmuir *et al.*, 1977; McKenzie & Bickle, 1988). We propose here that the melting mechanism is different at the great depths at which komatiites form (Fig. 11). At high pressure where the melt has approximately the same density as the solid, it does not escape and accumulates as it is produced. Only after the upwelling source reaches a depth of about 400 km (13 GPa) does the melt become buoyant and start to escape. This important limit is identified as the 'density limit' in Fig. 11.

From the trace-element composition of the Barberton komatiites, we infer that the proportion of liquid retained in the source at the density limit was high: between 30 and 50%. This is consistent with the source ascent paths proposed by Miller *et al.* (1991) and Herzberg (1995) for a komatiitic liquid erupting at ~1600°C. Under these conditions, the source consisted of a matrix of olivine and garnet crystals and a large proportion of interstitial silicate liquid. When the source rose to the depth at which the density limit was reached and the melt became positively buoyant, the melt would have begun to segregate and flow upwards to the surface. As is shown in Fig. 12, we infer that melt segregation started slowly and then accelerated rapidly, as the density contrast increased, to leave a solid residue that retained very little melt (probably less than 1% because of the low melt productivity of the
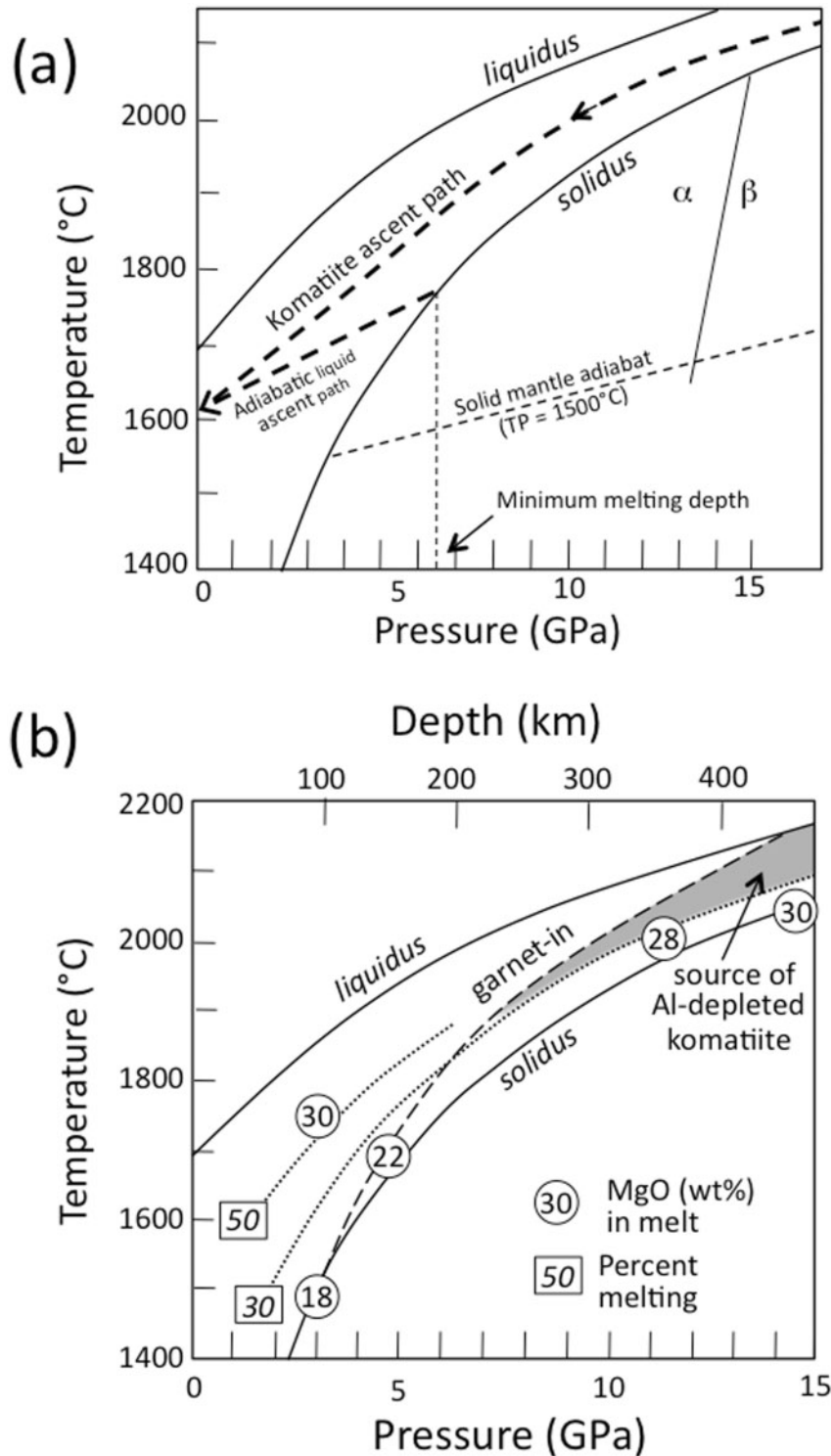
Fig. 10. (a) Portion of the peridotite phase diagram modified from Herzberg & Zhang (1996), illustrating possible ascent paths for komatiite liquids. The adiabatic liquid ascent path, projected downwards from the eruption temperature at 1600°C, gives the minimum melting depth for a near-solidus liquid. Komatiites form at higher degrees of melting and their ascent path must be more like the curved dashed path. Also shown is the transition from α to β olivine (wadsleyite). At a pressure of 14 GPa, the hot komatiite source is in the α olivine field whereas cooler ambient mantle is in the β olivine field. (b) Peridotite phase diagram modified from Herzberg & Zhang (1996), showing the MgO contents of liquids produced at the solidus and at higher degrees of melting. The requirement that Al-depleted komatiite liquids contain 30% MgO and formed under conditions in which garnet was retained in the residue places their origin in the triangular grey field.
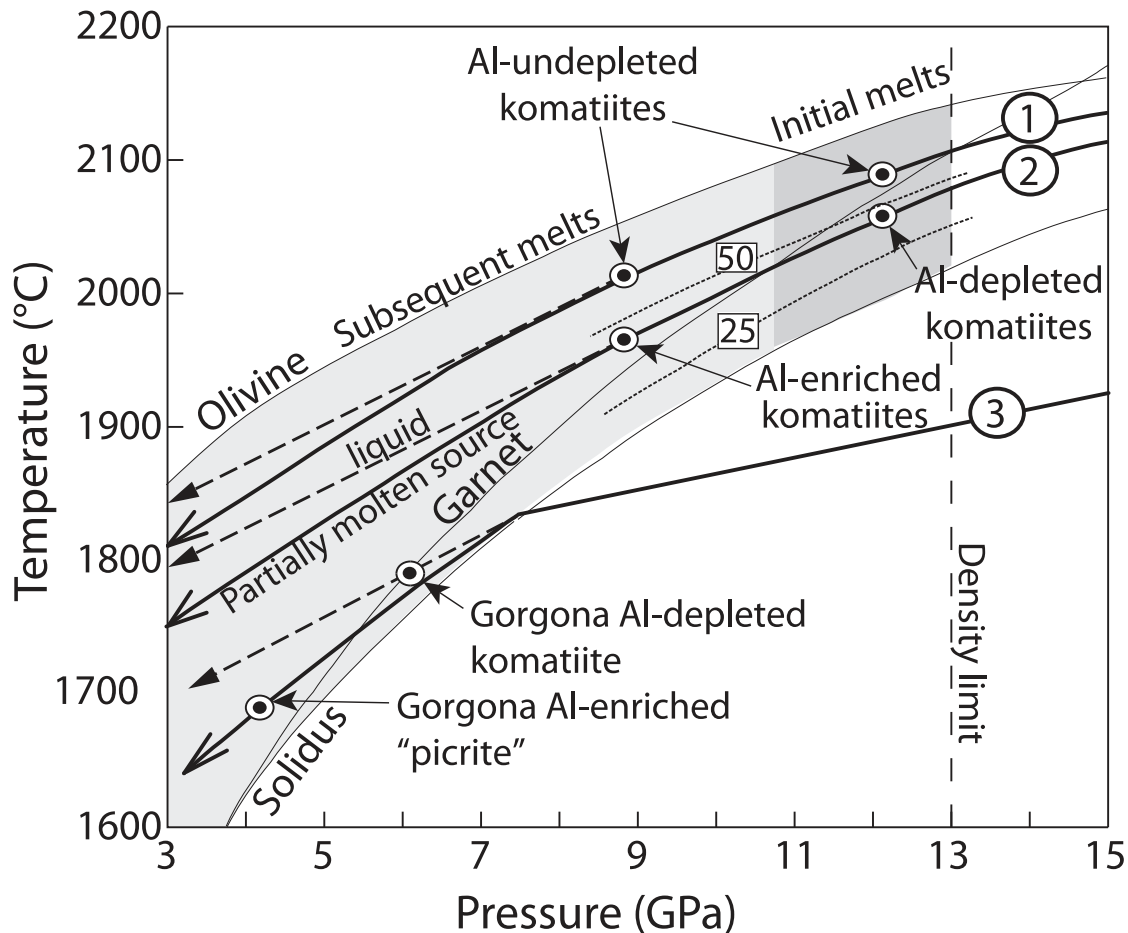
Fig. 11. Peridotite phase diagram showing the conditions of formation of various types of komatiite. Path 1 is that of a high-temperature plume that yields Al-undepleted komatiite through advanced critical melting. Path 2 is a slightly cooler plume that produces Al-depleted komatiite as a batch melt that is released after the source passes the density limit, and Al-enriched komatiite through continued melting of the refractory residue. Path 3 is that of a younger, cooler plume that produces first Al-depleted then Al-enriched komatiite at shallower depths.

now-refractory source). The melting situation thereby evolves from an early stage that is similar to batch melting, as the first melt separates from the source, to a late stage resembling advanced critical melting. The first liquid escaped during a process we will refer to as 'high-retention critical melting'.

Lee *et al.* (2010) have suggested that melt generated in the pressure interval 10–12 GPa would sink because of its high density, to accumulate in the lower part of the upper mantle. This process is thought to have occurred in the first billion years of Earth history to form a deep reservoir enriched in Fe and in incompatible trace elements. Lee *et al.* (2010) modelled low-degree partial melting that produces liquids that trickle down or percolate up through a mainly solid matrix, a process very different from that which generates komatiite magma. The constraints discussed above indicate that komatiite magmas formed by high-degree melting under conditions in which a large volume of melt coexisted with a disaggregated matrix.

In such a situation, the melt would indeed be denser than one of the residual phases (olivine), but would remain less dense than the other (garnet). It is important to recognize that melting does not take place under static conditions but occurs as a result of decompression in an ascending source. The source rises because the average density of the three phases—melt, olivine and garnet—is less than that of far-cooler ambient mantle.

It is possible that the three phases segregated within the melting zone of the plume to form a layer rich in melt that lagged behind less-dense olivine but moved ahead of garnet. The critical question—whether the melt ascended or descended relative to the surrounding mantle—depends on the density difference between that of the melt itself and that of the cooler ambient mantle. A simple calculation suggests it was less dense. Using data from Agee (1998), Suzuki *et al.* (1998) and Stixrude & Lithgow-Bertelloni (2010) we can estimate that at the conditions of formation of Al-depleted komatiite at 13 GPa
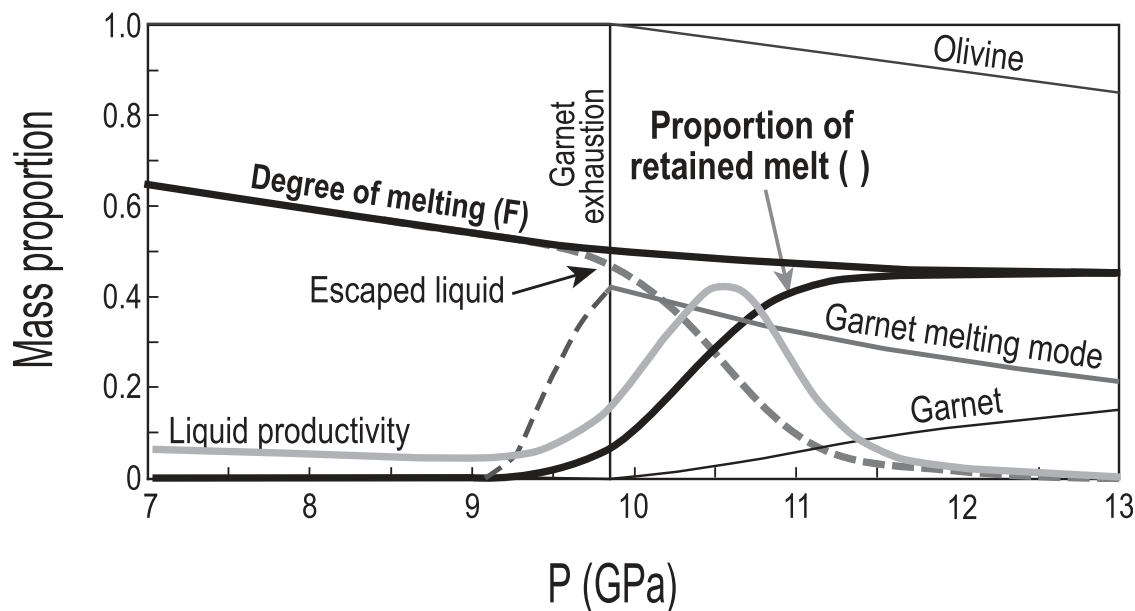
Fig. 12. Melting model for a source that produces 45% melt at 13 GPa. Curves labeled 'Olivine' and 'Garnet' represent the proportion of these minerals in the solid residue. The curve labeled 'Garnet melting mode' shows the proportion of garnet entering the melt, and the proportion in the trapped liquid after garnet exhaustion. The curves labeled 'Degree of melting (*F*)' and 'Escaped liquid' are expressed in proportion of the total initial source. The curve labeled 'Proportion of retained melt (φ)' is expressed in proportion of the evolving mass of the total source including solid residue and trapped liquid. The curve labeled 'Liquid productivity' represents the rate at which melt escapes the source, expressed as a proportion of the total initial source per GPa of ascent. Further explanation is given in the text in the section 'Melting model'.

and 2000°C, the densities of the coexisting phases within the plume were olivine (Fo$_{94}$) $3 \cdot 4 \, \text{g cm}^{-3}$, garnet $3 \cdot 7 \, \text{g cm}^{-3}$ and komatiite melt $3 \cdot 55 \, \text{g cm}^{-3}$. The ambient mantle at this depth was about 400°C cooler than the hot komatiite source and contained more Fe-rich olivine (Fo$_{90}$) and garnet. Another important factor that must be taken into account is the change from α to β olivine (wadsleyite), which takes place between about 13 and 15 GPa, depending on the temperature. As shown in Fig. 10a, the positive slope of this phase boundary means that olivine in the hot source of komatiites may have transformed to α olivine at 13 GPa whereas that in cooler ambient mantle remained as the β phase. The density of β olivine is about the same as that of garnet, at $3 \cdot 8 \, \text{g cm}^{-3}$, a value significantly greater than that of all phases in the hotter mantle plume, including the silicate liquid ($3 \cdot 55 \, \text{g cm}^{-3}$). On this basis we conclude that the melt would indeed be carried upwards within the rising plume until it reached the density limit when it escaped to the surface.

To model this process rigorously is not trivial because it requires monitoring of the production and properties of melt and residual solid within a mantle source that rises through the transition zone to the level at which the melt escapes. To do this properly requires consideration of the changing proportions, densities and distribution of all phases (melt, α and β olivine, and garnet), the phase changes in the plume and surrounding mantle, and the

complex geometry and dynamics of the mantle source. A complete treatment of the process is beyond the scope of this paper, but is under way, and will be published in a later paper (Schmeling & Arndt, in preparation).

Melting model

We modelled the evolution of the mineralogy of the komatiite source during its ascent from depths near the Transition Zone where melting is presumed to have started. Using the 14 GPa experiments of Takahashi (1986) and Ita & Stixrude (1992), we estimated that the peridotite source initially contained 64% olivine, 18% clinopyroxene and 18% majoritic garnet. Our modelling begins at 13 GPa, which is taken as the density limit where the first liquids leave the source. For the Barberton komatiites, melting started at the base of the upper mantle or in the lower mantle and probably reached about 30% at the density limit (Miller *et al.*, 1991; Herzberg, 1995; Fig. 10b). Clinopyroxene had totally entered the melt at this stage and the solid residue contained about 85% olivine and 15% majoritic garnet.

We calculated the degree of melting (*F*) as a function of pressure using an equation similar to that of Miller *et al.* (1991) but modified to fit better the more accurate mantle phase diagram of Zhang & Herzberg (1994). First, based on Zhang & Herzberg (1994), we assumed an appropriate *P–T* ascent path (Fig. 10a). Then we made the approximation that, at constant pressure, *F* is a linear function of

T between the solidus and the liquidus. This approximation does not take into account the decrease of melt productivity as the melting proceeds, a result of the exhaustion of garnet, the most fusible phase. McKenzie & Bickle (1988) proposed a polynomial expression of F as a function of T between the solidus and liquidus that takes into account this decrease of melt productivity and fits the experimental data between 0 and 5 GPa; however, Iwamori *et al.* (1995) showed that their expression is not valid at greater pressure, and that any proposed expression of F vs T would have to be variable with P to fit the experimental data up to 9 GPa. Moreover, no experimental constraints are available on F vs T between the liquidus and the solidus deeper than 9 GPa. Thus, we used a linear approximation that is close to Iwamori *et al.*'s (1995) polynomial solution and is easier to handle in the model. From this linear approximation and the P–T ascent path assumed in Fig. 10a, we obtained the expression

$$F = 0 \cdot 0055^* P^2 - 0 \cdot 1431^* P + F_{13\mathrm{GPa}} + 0 \cdot 931 \quad (1)$$

where $F_{13\mathrm{GPa}}$ is the degree of melting at 13 GPa.

We estimated the garnet melting mode (Υ_{Gt}) by dividing the proportion of garnet in the peridotite source (X_{Gt}) by the degree of melting at which the phase is exhausted ($F_{\mathrm{Gt\text{-}out}}$) during isobaric equilibrium melting, assuming a linear increase of F with T between solidus and liquidus:

$$\Upsilon_{\mathrm{Gt}} = X_{\mathrm{Gt}}/F_{\mathrm{Gt-out}}. \quad (2)$$

This is only an approximation because of the presence of three phases—olivine, majoritic garnet and clinopyroxene—in the source peridotite, but it takes into account the progressive shrinkage of the garnet stability field owing to the pressure decrease as the source rises. This expression calculates Υ_{Gt} as in batch melting, which is an acceptable approximation for our high melt retention critical melting model because the olivine + garnet + liquid cotectic position does not change significantly in olivine–garnet–clinopyroxene normative space as the bulk system (source + liquid) composition is changed by liquid extraction. From the phase diagram of Zhang & Herzberg (1994; Fig. 10)

$$F_{\mathrm{Gt-out}} = 0 \cdot 0082^* P^2 - 0 \cdot 0563^* P + 0 \cdot 1797. \quad (3)$$

Therefore, for the garnet melting mode, we propose the expression

$$\Upsilon_{\mathrm{Gt}} = X_{\mathrm{Gt}}/\left(0 \cdot 0082^* P^2 - 0 \cdot 0563^* P + 0 \cdot 1797\right) \quad (4)$$

where P is the pressure in GPa.

Parameters that allow calculation of the weight-proportion of retained melt (φ) in the mantle source have not been constrained experimentally or by theoretical models, so we had to infer the variation of φ with depth and pressure. Our approach was to choose a $\varphi(P)$ function that would (1) respect first-order physical constraints and (2) reproduce the trace-element spectra of the Barberton komatiites. As can be seen in Fig. 13, we choose an error-function expression that gives an 'S'-shape to the curve. This shape is based on the idea that between ~13 and 10 GPa, the progressive increase in density difference between solid and liquid initially results in accelerated segregation of liquid from solid, followed at lower pressure by stabilization at a lower value (<1%) because of the decrease in the permeability and the liquid production rate owing to the increasingly refractory character of the source. We therefore propose the expression

$$\varphi = \left(\frac{2}{g^*\sqrt{\pi}} * \int_0^{P/(j-h)} \mathrm{e}^{-t^2} * \mathrm{d}t\right) + i \text{ or } \varphi = \mathrm{erf}[P/(j-h)]/g + i$$

$$(5)$$

where g, h, i and j are numerical values chosen to define the shape of the curve. Their values are reported in Electronic Appendix 3.

We modelled the evolution of the source mineralogy at successive decompression steps of 0·05 GPa, which correspond to an increase of F from 0·002% to 0·2%, depending on the pressure. At each increment, depending on the F increase and the φ decrease, we calculated the quantity of liquid extracted from the source (X) and the incremental depletion in the source for each mineral phase via their melting modes. All results were expressed in mass proportion of the initial source and normalized to the declining mass of the solid source so that they could be represented in Fig. 12. We neglected the proportion of garnet that is lost during the decompression through the solid–solid reaction garnet → clinopyroxene + olivine. This proportion should be low, given that garnet is totally exhausted between 13 and ~9 GPa, and given the roughly constant proportion of garnet determined by Ita & Stixrude (1992) in this pressure range.

The trace-element composition of the source was calculated using the partition coefficients listed in Table 7, assuming $\mathrm{Lu/Hf_N} = 1\cdot06 \pm 2$ [where the subscript N indicates a value normalized to the primitive mantle of McDonough & Sun (1995)] and $\mathrm{Sm/Nd_N} = 1\cdot05 \pm 1$, as proposed by Blichert-Toft & Puchtel (2010) for the depleted mantle source of Archean komatiites. To reproduce such a source, we used a weighted average of 35% depleted mantle of Salters & Stracke (2004) and 65% primitive mantle of McDonough & Sun (1995) (Table 8).

We modelled trace-element concentrations assuming equilibrium between the melt retained in the source and the residue. To do this, we used the batch-melting equation of Shaw (1970):

$$C_{\mathrm{liq}} = \frac{C_0}{D_0 + F^*(1 - P)} \quad (6)$$

where C_{liq} is concentration in the liquid; C_0 is initial concentration in the source; $D_0 = \Sigma X_i^* K_{\mathrm{D}i}$, where X_i is the
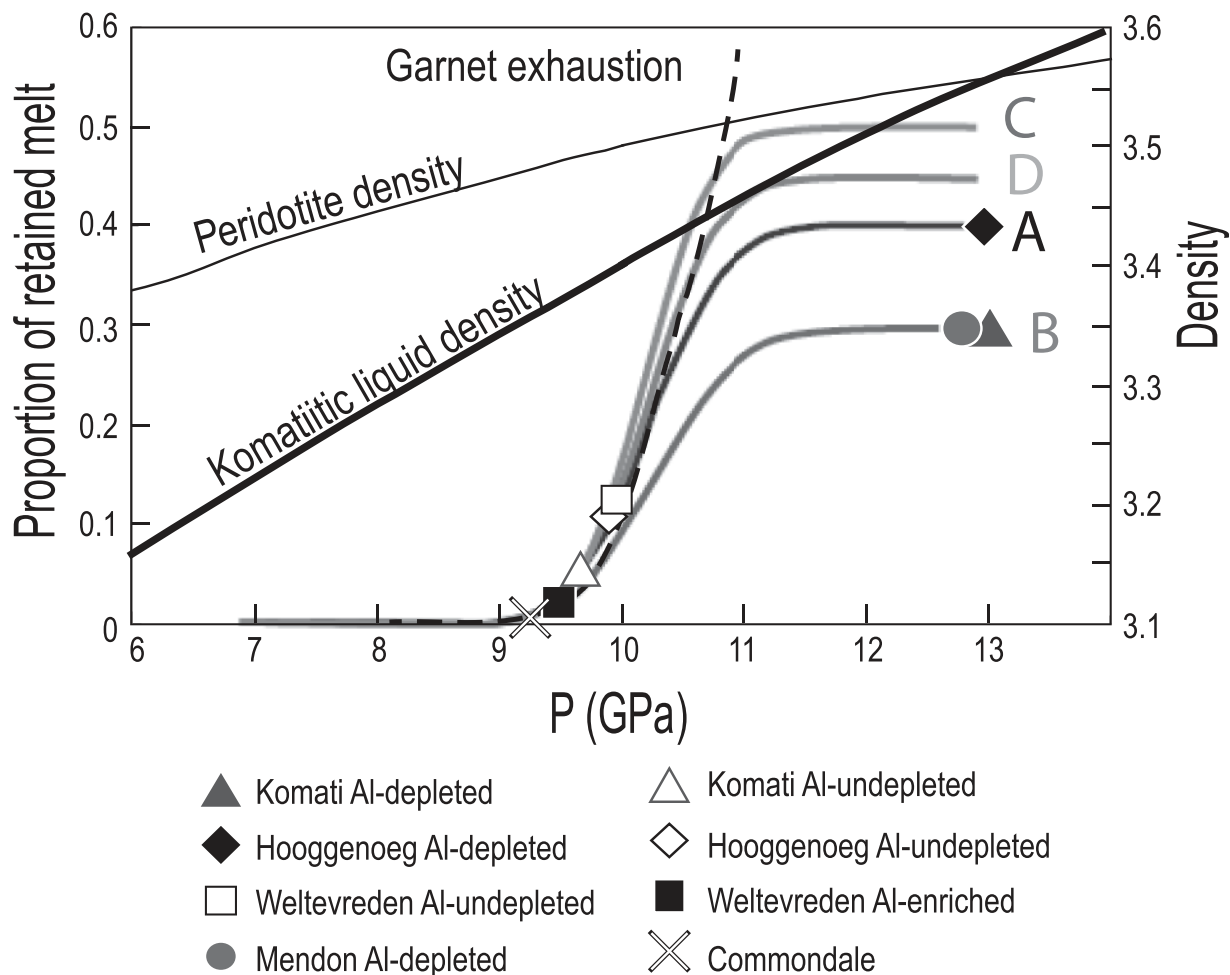
Fig. 13. Proportion of retained melt (φ) vs pressure (GPa) for the four modeled P–T ascent paths corresponding, at 13 GPa, to the following degrees of melting: A, 30%; B, 40%; C, 45%; D, 50%. The symbols corresponding to each komatiite type represent the loci at which their parental magma escaped its source. The density curves are from Agee (1998).

proportion of the phase i in the source and K_{Di} is the partition coefficient of the considered element between the phase i and the liquid; partition coefficients are from Borg & Draper (2003; Table 7).

Temperatures in the sources of komatiites vary because some plumes are hotter than others and each plume has a hotter center and a cooler periphery. For this reason, we modeled melting along several different ascent paths corresponding to different temperatures (prior to the beginning of the fusion) of the sources. To express the temperature (T_s) of the source, we used the temperature at the density limit at 13 GPa. This temperature controls the degree of melting at the density limit (which we will refer to as F_{13GPa}; e.g. on the ascent path 2 of Fig. 11, it corresponds to $F_{13GPa} \sim 0{\cdot}3$ or 30% melting). Further discussion of the model parameters and solutions can be found in Electronic Appendix 3. Spreadsheets of the trace-element calculations are available from the author.

Model results

Figure 14 shows that high-melt retention critical melting produces liquids with trace-element patterns that are intermediate between fractional and low-retention critical melting on the one hand and batch melting on the other hand. At the same degree of melting, the patterns are less fractionated with higher absolute concentrations than the former, and a little more fractionated with lower absolute concentrations than the latter. Figure 14 shows the evolution of the trace-element pattern of the total source (i.e. solid residue + retained liquid) and of the liquid that is extracted from the source.

The first liquids extracted at the greatest depths are in equilibrium with a source containing abundant residual garnet (e.g. liquids extracted from the grey area in Fig. 10b) and they are HREE depleted, as shown in Fig. 14b. As the source rises and the melting proceeds, garnet is progressively depleted in the residue, and the

Table 7: Mineral–melt partition coefficients used in the model (Borg & Draper, 2003)

	D_{Gt}	D_{Ol}
Th	0·0001	0·0001
Nb	0·0051	0·0003
La	0·0100	0·0004
Ce	0·0210	0·0005
Nd	0·0360	0·0010
Sm	0·1030	0·0013
Eu	0·2200	0·0016
Gd	0·4300	0·0015
Tb	0·3350	0·0015
Dy	0·4700	0·0017
Y	1·0100	0·0016
Er	0·7900	0·0015
Tm	1·1800	0·0015
Yb	1·5900	0·0015
Lu	1·9300	0·0015

Partition coefficient for Nb was taken as the average of Th and La.

Table 8: Trace-element compositions (in ppm) of the source used in our model, the primitive mantle, depleted mantle and the continental crust used as contaminant

	Source used in our model	Primitive mantle (McDonough & Sun, 1995)	Depleted mantle (Salters & Stracke, 2004)	Contaminating continental crust (Drummond *et al.*, 1996)
Th	0·06	0·08	0·01	6
Nb	0·50	0·66	0·21	5·4
La	0·50	0·65	0·23	29·8
Ce	1·36	1·68	0·77	51·6
Nd	1·06	1·25	0·71	19·9
Sm	0·36	0·41	0·27	2·7
Zr	9·60	10·5	7·94	–
Hf	0·25	0·28	0·20	–
Eu	0·14	0·15	0·11	0·91
Ti	1063	1205	798	1978
Gd	0·49	0·54	0·40	2·04
Tb	0·09	0·10	0·08	0·25
Dy	0·62	0·67	0·53	1·16
Y	4·22	4·30	4·07	6·8
Er	0·41	0·44	0·37	–
Tm	0·07	0·07	0·06	–
Yb	0·43	0·44	0·40	0·46
Lu	0·07	0·07	0·06	0·09

extracted liquids become less and less HREE depleted until at $F \sim 0.5$ garnet is exhausted and subsequent melts are no longer HREE depleted. From then on (e.g. for path 2 in the shaded zone labeled 'subsequent melts' in Fig. 11), only olivine enters the melt and the trace-element concentrations of the melt decrease because of continued extraction of liquids, which progressively depletes the source. Figure 15 shows the evolution of critical trace-element ratios during melting for four paths corresponding to sources with differing temperatures for which F_{13GPa} is 0·3, 0·4, 0·45 and 0·5.

At first, owing to progressive extraction of garnet from the source, the Gd/Yb$_N$ ratio of the liquid decreases rapidly but with little decrease of La/Sm$_N$ and little change in the overall absolute trace-element concentrations (represented by normalized Gd concentrations in Fig. 15c and d), because φ is high and buffers the source depletion. As the source ascends, φ decreases (Fig. 12), the buffering effect of the retained melt declines, and both the La/Sm$_N$ ratio (Fig. 15a and b) and absolute trace-element concentrations (Fig. 15c and d) decrease ever faster. After garnet exhaustion, as shown for the $F_{13GPa} = 0.45$ and $F_{13GPa} = 0.5$ curves in Fig. 15, the Gd/Yb$_N$ ratio changes little, and only La/Sm$_N$ and absolute trace-element concentrations keep decreasing.

Model solutions
As discussed above, Al-depleted komatiites form at higher pressure and at a lower degree of melting than

Al-undepleted and Al-enriched komatiites. To explain these differences we propose that the former are produced during the early deep stages of melting (e.g. for path 2, in the 'initial melt' zone in Fig. 11), and the latter during the subsequent melting at shallower depths (for paths 1 and 2, in the 'subsequent melts' zone in Fig. 11). The justification for this model is given in Fig. 16, which shows the best fits between measured and model trace-element spectra. In each diagram, the spectrum representing the measured data is the average concentrations of all samples, normalized to the MgO content of the parental magma. It reproduces the parental magma trace-element spectrum within ∼15% (taking into account uncertainties such as the analytical error, the error on the MgO content of the parental liquid, on the Mg# of the accumulated olivine, etc.). The estimated uncertainty on the model spectra (taking into account the errors on the different parameters of the model) is ∼10% for the LREE and a little higher (15–20%) at great depth for HREE because of the uncertainty on garnet partition coefficients and abundance in the residue. Figure 11 shows the loci of melting for each komatiite type in *P–T* space. To reproduce the diversity of
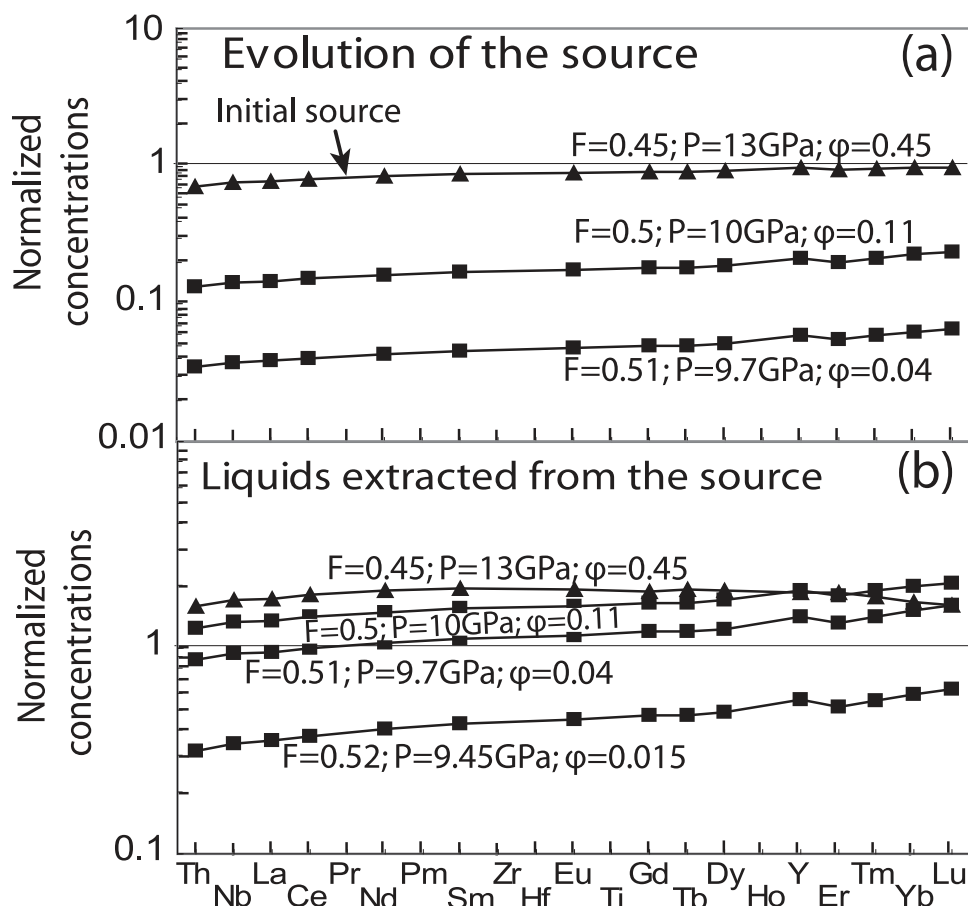
Fig. 14. Model trace-element spectra for the extracted liquids and the source (solid residue + retained liquid). The source composition is that of Fig. 13; it produces 0·45% melt at 13 GPa. The uppermost curve shows the composition of the batch melt extracted as the source passes the neutral buoyancy level; the lower curves show the evolution of fractional melts produced by continued melting of the residue.

the Barberton komatiites, we had to model four source potential temperatures respectively corresponding to 30, 40, 45 and 50% of melting at 13 GPa. For each komatiite type, the source potential temperature can be estimated, because only one of the four source potential temperatures that we modelled reproduces their trace-element characteristics.

Figure 16a shows that the trace-element spectra, and particularly the strong HREE depletion, of the Al-depleted komatiites, are best matched by the first liquids to escape at ~13 GPa from sources with moderately elevated temperatures that produced 30–40% melting at this pressure. Under these conditions, garnet was retained in the residue to cause the HREE depletion.

For Al-undepleted and Al-enriched komatiites, the best fits are melts extracted at shallower depths and at higher degrees of melting from sources that had been depleted by the segregation of early formed melts. The flat HREE and the slightly depleted LREE patterns of the Al-undepleted komatiites are best reproduced with an extremely high source temperature that resulted in 50% melting at 13 GPa. According to our model, little garnet remains under these conditions and it is soon exhausted, and the high proportion of retained melt mitigates the fractionation of HREE between liquid and residue while garnet remains in the residue. Therefore, melts that are extracted at this stage are only very slightly depleted with respect to the residue, and after garnet is totally exhausted the extracted liquids have essentially the same REE ratios as the residue. As a result, all melts produced from such an extremely hot source have flat HREE patterns. The *P–T* conditions at the point of melt extraction are above the garnet-out curve (Fig. 11) and correspond to depths at which the proportion of retained melt has fallen to 4–12% (Figs 12 and 16).

The trace-element spectra of Al-enriched komatiites, with their enriched HREE, are best reproduced with an intermediate source temperature, corresponding to ~45% of melting at 13 GPa. In this case, the proportion of retained melt was lower, and garnet was retained longer
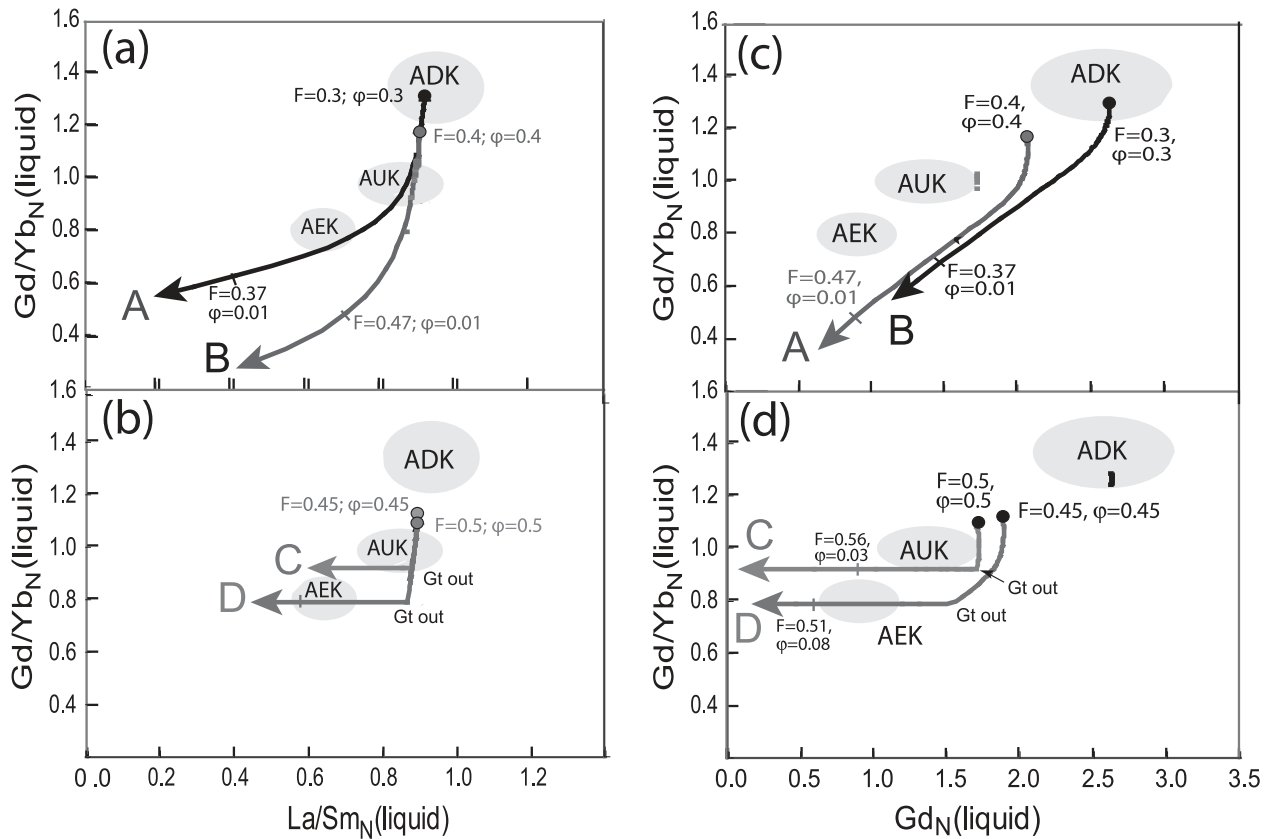
Fig. 15. Evolution of the liquid composition through the fusion for the four modeled $P–T$ ascent paths corresponding, at 13 GPa, to the following degrees of melting: A, 30%; B, 40%; C, 45%; D, 50%. Along the melting paths, curves are labeled with the degree of melting (F) and the corresponding proportion of retained melt (φ). Points labeled 'Gt out' are garnet exhaustion points. ADK, Al-depleted komatiite; AUK, Al-undepleted komatiite; AEK, Al-enriched komatiite.

and in higher proportion in the residue. As a consequence, the HREE in the extracted liquids were more strongly depleted with respect to the residue and the depletion persisted to higher degrees of melting. Therefore, they left a residue with a HREE-enriched pattern that was transmitted to the subsequently extracted liquids. The locus of melting is past the garnet-out curve and corresponds to the stage when the proportion of retained melt has decreased to around 2%.

Comparison of the major-element compositions of the parental komatiitic magmas with Herzberg's (2004) extrapolated melting model produces an acceptable match and supports these conditions of melting.

Refinements to the model

Garnet segregation during melting. Green (1975), Ohtani (1984) and Arndt *et al.* (2008) have proposed that partially molten sources containing a high proportion of retained liquid at great depth may have undergone some internal differentiation when denser garnet partially separated and lagged behind the rest of the source. This extraction of garnet might have contributed to the Al_2O_3 and HREE depletion of the Al-depleted komatiites. In addition,

enrichment in garnet in deeper parts of the source could have contributed to the relatively high Al_2O_3 and HREE of the Al-enriched type of komatiites. These effects have not been taken into account in our model.

Contamination by the continental crust. Two groups of komatiites display trace-element evidence of contamination by continental crust. The Al-depleted komatiites from spinifex horizon 1 and from the Mendon Formation have LREE-enriched patterns, large Nb negative anomalies and negligible Zr–Hf anomalies—features of magmas that have assimilated crustal rocks (Fig. 16c and d). To model this contamination, we used the average Archean granitoid of Drummond *et al.* (1996) to represent the contaminant. For simplicity we assumed that the liquid was superheated and that the contamination was not accompanied by crystallization. As can be seen in Fig. 16c and d, the LREE patterns of the liquid are consistent with 2·5–3% of contamination.

High field strength element anomalies. Figures 5 and 16 show that most Barberton komatiites have negative HFSE anomalies. In the case of Nb, when contamination by
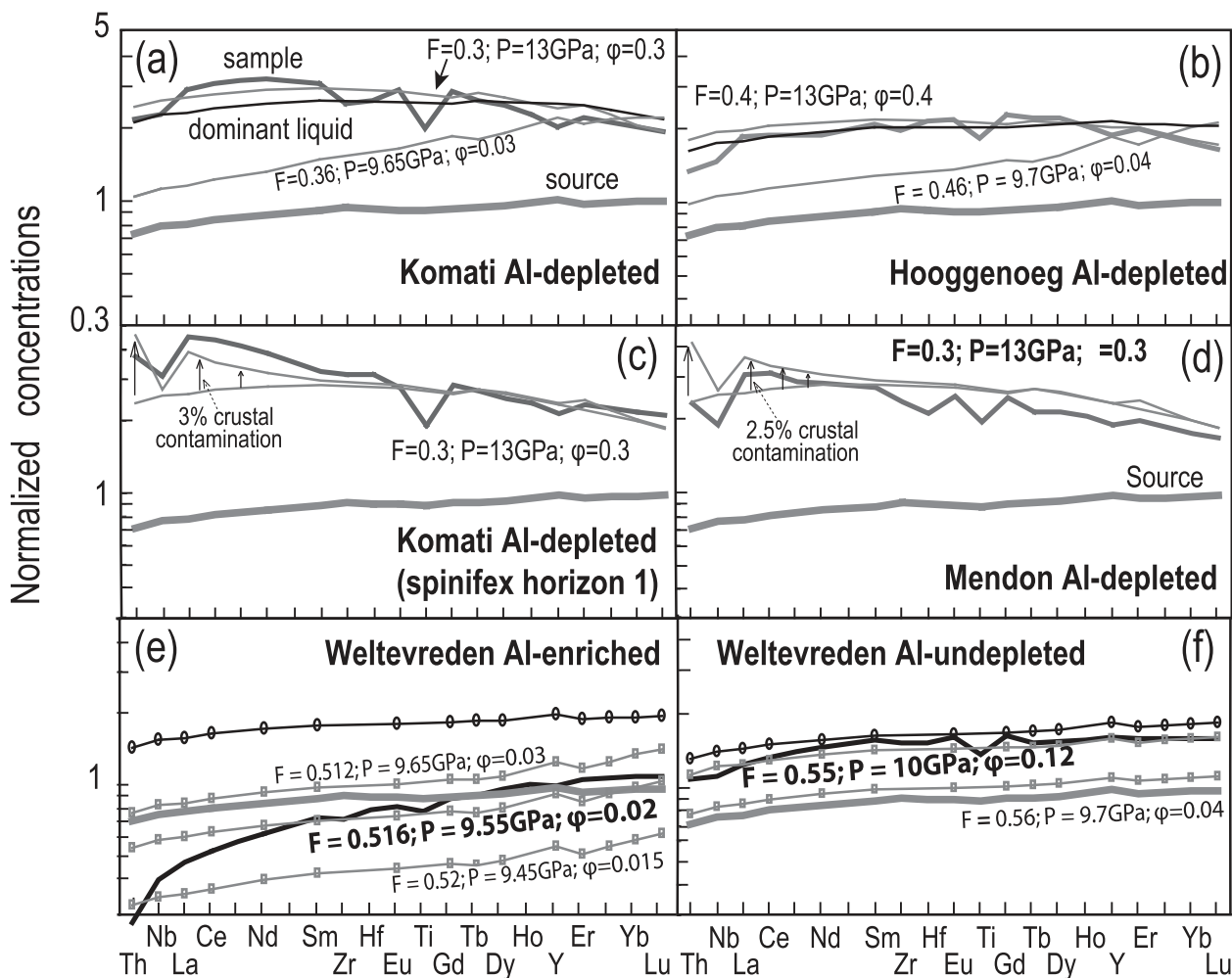
Fig. 16. Modelled best-fit solutions for each komatiite type. Unlabelled bold spectra are the averages of the measured concentrations. The fine grey lines represent, in each case, the dominant spectrum among the liquids produced. They correspond to the liquids produced at the liquid productivity peak in Fig. 12. Concentrations are normalized to primitive mantle from McDonough & Sun (1995).

continental crust occurred, this anomaly is superimposed on the negative anomaly owing to the contamination (Fig. 16). We considered three possible explanations for the HFSE anomalies, as follows.

(1) They are due to garnet subtraction from the sources or from the liquids. These elements have been proposed to be compatible in garnet by some workers (Dasgupta et al., 2009) but this interpretation is not unanimously accepted (Borg & Draper, 2003; Corgne & Wood, 2004). We reject this explanation for the anomalies in the Barberton komatiites because they are not systematically coupled with HREE depletion, as would be expected from a garnet-depleted source or magma. For example, they are most pronounced in Al-undepleted samples from the Komati Formation, which have flat HREE patterns.

(2) They result from alteration. As discussed above, both the REE and the HFSE are relatively immobile and

there is no obvious correlation between the size of the anomaly and the degree of alteration, as inferred from petrography or from the scatter of more mobile trace elements such as the LILE.

(3) They are a source feature that is not related to garnet. Unlike other trace elements, Th, Nb, Zr, Hf and Ti are compatible with Mg-perovskite (Kato et al., 1988, 1996; Taura et al., 2001; Corgne et al., 2005) and negative Zr, Hf and Ti anomalies could have been caused by earlier segregation of this mineral (Jochum et al., 1991; Xie et al., 1993).

Worldwide variability of komatiites explained by the model

Al_2O_3/TiO_2 ratios

The Al_2O_3/TiO_2 ratio, which forms the basis of the nomenclature for komatiites, is controlled by three factors.

The first is the Al_2O_3/TiO_2 ratio of the source. Because Al is more compatible than Ti, depleted mantle has a higher Al_2O_3/TiO_2 ($\sim$32; Salters & Stracke, 2004) than primitive mantle ($\sim$22; McDonough & Sun, 1995). For a moderately depleted mantle source, as used in the model, $Al_2O_3/TiO_2 \sim 25$. The two other factors are the source temperature prior to the beginning of melting, and the degree and mechanism of melting.

Sources with very high temperatures (e.g. path 1 in Fig. 11) do not produce Al-depleted komatiites because, by the time the source reaches the neutral density limit at $\sim$13 GPa, garnet is already close to exhaustion in the residue and the large proportion of retained melt limits the fractionation of Al_2O_3 relative to TiO_2 between the liquid and the residue. Therefore, komatiites produced from such very hot sources have roughly the same Al_2O_3/TiO_2 ratio as their sources. If their sources are primitive or little depleted (as is the case for Barberton komatiites) Al_2O_3/TiO_2 ratios will be around the primitive mantle value ($\sim$22): the komatiites will be Al-undepleted. If the sources are more depleted, Al_2O_3/TiO_2 will be higher: the komatiites will be Al-enriched (for a source as depleted as present-day depleted mantle, Al_2O_3/TiO_2 ratios will be $\sim$30).

Sources with lower temperatures (e.g. path 2 in Fig. 11), but still hot enough for melting to have started at depths at which garnet is retained in the residue (roughly $>$ 7 GPa), produce Al-depleted komatiites. The escape of these liquids, which have low Al_2O_3/TiO_2, leaves a residue with high Al_2O_3/TiO_2; therefore, subsequent melting of the residue produces Al-enriched komatiites.

Still cooler sources (e.g. path 3 in Fig. 11) do not begin to melt until they reach shallower depths where garnet is stable only close to the solidus (roughly $P < 7$ GPa). During a short interval of melting, under conditions near the solidus, they first produce Al-depleted meimechite (an ultramafic liquid highly enriched in incompatible elements with a strongly fractionated REE pattern; Arndt *et al.*, 1998; Elkins-Tanton *et al.*, 2007), and then Al-undepleted to slightly Al-enriched komatiites.

Examples of komatiites from other greenstone belts

The most common type of komatiite is the $\sim$2·7 Ga Al-undepleted variety, as found in the Munro Township in the Abitibi Greenstone Belt, Canada (Pyke *et al.*, 1973; Arndt, 1986). Their near-chondritic Al_2O_3/TiO_2 ratios and flat HREE patterns could have been produced either from very hot sources like path 1 in Fig. 11, or by relatively cool sources, close to or after garnet exhaustion, like path 3. However, their depleted LREE patterns, together with their relatively high middle REE (MREE) and HREE concentrations, cannot be reproduced from a very hot source, because the REE concentrations in the extracted liquids fall to too low values before the LREE become significantly fractionated. Therefore, Munro-type komatiites

were probably produced from relatively cool sources (between paths 2 and 3 in Fig. 11).

The Commondale Greenstone Belt, located $\sim$30 km SW of the Barberton belt, contains komatiites with extremely depleted and fractionated REE patterns and extremely high Al_2O_3/TiO_2 ratios (from 60 to 74; Wilson, 2003). These characteristics can be reproduced by our model using a relatively cool source and a degree of melting of $\sim$40% (Electronic Appendix 4).

The only Phanerozoic komatiites are found on Gorgona Island off the Colombian Pacific coast (Echeverría, 1980). These komatiites are very similar to Munro Al-undepleted komatiites in that they have flat to slightly HREE depleted, strongly LREE depleted patterns, and chondritic to slightly subchondritic Al_2O_3/TiO_2 ratios. The island also contains so-called 'picrites', which match the geochemical definition of komatiites but lack spinifex textures. These rocks have a stronger LREE depletion, more enriched HREE and $Al_2O_3/TiO_2 \sim 30$ (Révillon *et al.*, 2000). Their calculated parental magmas have only slightly lower MgO contents (18–25%; Révillon *et al.*, 2000) than the Munro komatiites (20–28%; Arndt, 1977), which shows that they were produced either by a lower degree of melting or from a slightly cooler source ($\sim$path 3 in Fig. 11). Their strong depletion in highly incompatible elements (such as LREE and Ti; Révillon *et al.*, 2000) favours the latter. The first extracted liquids would have been Al-depleted meimechites, which are not found on the surface, perhaps because they were produced in low quantity. Komatiites formed close to the garnet exhaustion point, and finally the picrites were derived from the residue that had become strongly depleted by the extraction of meimechite and komatiite.

Secular evolution of komatiites

Throughout Earth history, the proportion of Al-depleted komatiites has progressively declined. They were relatively abundant in the early Archean when they erupted together with Al-undepleted and Al-enriched types, but became rare in the late Archean. Thereafter they disappeared, leaving only Al-undepleted and Al-enriched types in the Proterozoic and the single Phanerozoic komatiite occurrence (Gorgona Island). This decline, which coincided with a decrease in the overall abundance of komatiite, has long been attributed to secular mantle cooling (Herzberg, 1992, 1995; Nisbet *et al.*, 1993). This agrees well with the results of our model, which show that Al-depleted komatiites require a high source temperature that could have existed only early in Earth history, before the mantle cooled significantly. Only Al-undepleted and Al-enriched types were produced in the Proterozoic when the mantle was cooler, and in the Phanerozoic the mantle became too cool to produce komatiites, apart from some rare exceptions.

CONCLUSIONS

The Barberton Greenstone Belt contains three types of komatiite distinguished by different Al_2O_3/TiO_2 ratios and REE profiles. These types are commonly found in the same formation, which indicates that they formed synchronously. Their highly ultramafic compositions, together with their REE patterns, require that the parental magmas formed at great depth (>9 GPa). To explain the three types of komatiite we have developed a new model that depends on two critical factors: (1) at pressures greater than 13 GPa, the densities of melt and residual solid are similar; (2) as pressure decreases in a rising mantle source, the melt progressively escapes the source once the neutral density limit is reached. The various types of komatiite represent liquids that escape the source at different stages of the melting process.

Al-depleted komatiites, the most common and characteristic of the Barberton ultramafic lavas, formed under conditions of near-neutral buoyancy when a large proportion of melt (30–40%) was retained in the source in equilibrium with residual garnet. Al-undepleted komatiites from Barberton formed from a hotter source that released melt only after garnet was eliminated by high-degree melting. Al-enriched komatiite formed through melting of the refractory residue left after extraction of earlier melts in the presence of residual garnet. The model not only is valid for Barberton komatiites, but also can explain the characteristics of komatiites from Abitibi, Commondale, Gorgona, and other regions.

SUPPLEMENTARY DATA

Supplementary data for this paper are available at *Journal of Petrology* online.

REFERENCES

Agee, C. B. (1998). Crystal–liquid density inversions in terrestrial and lunar magmas. *Physics of the Earth and Planetary Interiors* **107**, 63–74.

Allègre, C. J. (1982). Genesis of Archaean komatiites in a wet ultramafic subducted plate. In: Arndt, N. T. & Nisbet, E. G. (eds) *Komatiites*. London: George Allen and Unwin, pp. 495–500.

Anhaeusser, C. R. (1985). Archean layered ultramafic complexes in the Barberton Mountain land, South Africa. In: Ayres, L. D., Thurston, P. C., Card, K. D. & Weber, W. (eds) *Evolution of Archean Supracrustal Sequences. Geological Association of Canada*, Special Papers 28, 281–301.

Armstrong, R. A., Compston, W., de Wit, M. J. & Williams, I. S. (1990). The stratigraphy of the 3·5–3·2 Ga Barberton Greenstone Belt revisited: A single zircon ion microprobe study. *Earth and Planetary Science Letters* **101**, 90–106.

Arndt, N. (2003). Komatiites, kimberlites, and boninites. *Journal of Geophysical Research* **108**, 2293.

Arndt, N. T. (1976). Melting relations of ultramafic lavas (komatiites) at 1 atm and high pressure. *Carnegie Institution of Washington, Yearbook 75*, 555–562.

Arndt, N. T. (1977). Thick, layered peridotite–gabbro lava flows in Munro Township, Ontario. *Canadian Journal of Earth Sciences* **14**, 2620–2637.

Arndt, N. T. (1986). Differentiation of komatiite flows. *Journal of Petrology* **27**, 279–301.

Arndt, N., Ginibre, C., Chauvel, C., Albarède, F., Cheadle, M., Herzberg, C., Jenner, G. & Lahaye, Y. (1998). Were komatiites wet? *Geology* **26**, 739–742.

Arndt, N. T., Lesher, C. M. & Barnes, S. J. (2008). *Komatiite*. Cambridge: Cambridge University Press.

Berry, A. J., Danyushevsky, L. V., O'Neill, H. S., Newville, M. & Sutton, S. R. (2008). Oxidation state of iron in komatiitic melt inclusions indicates hot Archaean mantle. *Nature* **455**, doi:10.1038/nature07377.

Blichert-Toft, J. & Arndt, N. T. (1999). Hf isotope compositions of komatiites. *Earth and Planetary Science Letters* **171**, 439–451.

Blichert-Toft, J. & Puchtel, I. S. (2010). Depleted mantle sources through time: Evidence from Lu–Hf and Sm–Nd isotope systematics of Archean komatiites. *Earth and Planetary Science Letters* **297**, 598–606.

Borg, L. E. & Draper, D. S. (2003). A petrogenetic model for the origin and compositional variation of the martian basaltic meteorites. *Meteoritics & Planetary Science* **38**, 1713–1731.

Byerly, G. R. (1999). Komatiites of the Mendon Formation: late-stage ultramafic volcanism in the Barberton greenstone belt. In: Lowe, D. R. & Byerly, G. R (eds) *Geological Evolution of the Barberton Greenstone Belt*. Boulder, CO: Geological Society of America, 329, pp. 189–212.

Byerly, G. R., Kröner, A., Lowe, D. R., Todt, W. & Walsh, M. M. (1996). Prolonged magmatism and time constraints for sediment deposition in the early Archean Barberton greenstone belt: evidence from the Upper Onverwacht and Fig Tree groups. *Precambrian Research* **78**, 125–138.

Campbell, I. H., Griffiths, R. W. & Hill, R. I. (1989). Melting in an Archaean mantle plume: heads it's basalts, tails it's komatiites. *Nature* **339**, 697–699.

Chauvel, C., Bureau, S. & Poggi, C. (2011). Comprehensive chemical and isotopic analyses of basalt and sediment reference materials. *Geostandards and Geoanalytical Research* **35**, 125–143.

Chavagnac, V. (2004). A geochemical and Nd isotopic study of Barberton komatiites (South Africa): implication for the Archean mantle. *Lithos* **75**, 253–281.

Connolly, B. D., Puchtel, I. S., Walker, R. J., Arevalo, R., Piccoli, P. M., Byerly, G., Robin-Popieul, C. & Arndt, N. T. (2012). HSE systematics of the 3.3 Ga Weltevreden komatiites, South Africa: implications for the early Earth's history. *Earth and Planetary Science Letters* (in press).

Corgne, A. & Wood, B. J. (2004). Trace element partitioning between majoritic garnet and silicate melt at 25 GPa. *Physics of the Earth and Planetary Interiors* **143**, 407–409.

Corgne, A., Liebske, C., Wood, B. J., Rubie, D. C. & Frost, D. J. (2005). Silicate perovskite-melt partitioning of trace elements and geochemical signature of a deep perovskitic reservoir. *Geochimica et Cosmochimica Acta* **69**, 485–496.

Cooper, M. R. (2008). Komatiitic flows of the Pioneer ultramafic complex of the 3·3 Ga Weltevreden Formation, Barberton greenstone belt, South Africa: stratigraphy, petrology, and geochemistry. Baton Rouge, LA: PhD thesis, Louisiana State University, 160 pp.

Dann, J. C. (2000). The 3·5 Ga Komati Formation, Barberton Greenstone Belt, South Africa, Part I: New maps and magmatic architecture. *South African Journal of Geology* **103**, 47–68.

Dann, J. C. (2001). Vesicular komatiites, 3.5-Ga Komati Formation, Barberton Greenstone Belt, South Africa: inflation of submarine lavas and origin of spinifex zones. *Bulletin of Volcanology* **63**, 462–481.

Danyushevsky, L. V. (2001). The effect of small amounts of H_2O on crystallisation of mid-ocean ridge and backarc basin magmas. *Journal of Volcanology and Geothermal Research* **110**, 265–280.

Dasgupta, R., Hirschmann, M. M., McDonough, W. F., Spiegelman, M. & Withers, A. C. (2009). Trace element partitioning between garnet lherzolite and carbonatite at 6·6 and 8·6 GPa with applications to the geochemistry of the mantle and of mantle-derived melts. *Chemical Geology* **262**, 57–77.

deWit, M. J., Roering, C., Hart, R. J., Armstrong, R. A., de Ronde, C. E. J., Green, R. W. E., Tredoux, M., Peberdy, E. & Hart, R. A. (1992). Formation of an Archaean continent. *Nature* **357**, 553–562.

Drummond, M. S., Defant, M. J. & Kepezhinskas, P. K. (1996). Petrogenesis of slab-derived trondhjemite–tonalite–dacite/adakite magmas. *Transactions of The Royal Society Edinburgh: Earth Sci.* **87**, 205–216.

Echeverría, L. M. (1980). Tertiary or Mesozoic komatiites from Gorgona Island, Colombia: Field relations and geochemistry. *Contributions to Mineralogy and Petrology* **73**, 253–266.

Elkins-Tanton, L., Draper, D., Agee, C., Jewell, J., Thorpe, A. & Hess, P. (2007). The last lavas erupted during the main phase of the Siberian flood volcanic province: results from experimental petrology. *Contributions to Mineralogy and Petrology* **153**, 191–209.

Green, D. H. (1975). Genesis of Archean peridotitic magmas and constraints on Archean geothermal gradients and tectonics. *Geology* **3**, 15–18.

Green, D. H., Sie, S. H., Ryan, C. G. & Cousens, D. R. (1989). Proton microprobe-determined partitioning of Nb, Ta, Zr, Sr and Y between garnet, clinopyroxene and basaltic magma at high pressure and temperature. *Chemical Geology* **74**, 201–216.

Grove, T. L., Parman, S. W. & Dann, J. C. (1999). Conditions of magma generation for Archean komatiites from Barberton mountainland, South Africa. In: Frei, Y., Bertka, C. M. & Mysen, B. O (eds) *Mantle Petrology: Field Observations and High-pressure Experimentation.* Houston, TX: The Geochemical Society, Special Publication No 6, pp. 155–167.

Gruau, G., Chauvel, C. & Jahn, B. M. (1990). Anomalous Sm – Nd ages for the early Archean Onverwacht Group Volcanics. *Contributions to Mineralogy and Petrology* **104**, 27–34.

Herzberg, C. (1992). Depth and degree of melting of komatiites. *Journal of Geophysical Research* **97**, 4521–4540.

Herzberg, C. (1995). Generation of plume magmas through time: An experimental perspective. *Chemical Geology* **126**, 1–16.

Herzberg, C. (2004). Geodynamic information in peridotite petrology. *Journal of Petrology* **45**, 2507–2530.

Herzberg, C. & Asimow, P. D. (2008). Petrology of some oceanic island basalts: PRIMELT2.XLS software for primary magma calculation. *Geochemistry, Geophysics, Geosystems* **9**, Q09001.

Herzberg, C. & O'Hara, M. J. (2002). Plume-associated ultramafic magmas of Phanerozoic age. *Journal of Petrology* **43**, 1857–1883.

Herzberg, C. & Ohtani, E. (1988). Origin of komatiite at high pressures. *Earth and Planetary Science Letters* **88**, 321–329.

Herzberg, C. & Zhang, J. (1996). Melting experiments on anhydrous peridotite KLB-1: Compositions of magmas in the upper mantle and transition zone. *Journal of Geophysical Research* **101**, 8271–8295.

Herzberg, C., Condie, K. & Korenaga, J. (2010). Thermal history of the Earth and its petrological expression. *Earth and Planetary Science Letters* **292**, 79–88.

Hofmann, A. W. (1988). Chemical differentiation of the Earth: the relationship between mantle, continental crust, and oceanic crust. *Earth and Planetary Science Letters* **90**, 297–314.

Inoue, T., Rapp, R. P., Zhang, J., Gasparik, T., Weidner, D. J. & Irifune, T. (2000). Garnet fractionation in a hydrous magma ocean and the origin of Al-depleted komatiites: melting experiments of hydrous pyrolite with REEs at high pressure. *Earth and Planetary Science Letters* **177**, 81–87.

Ita, J. & Stixrude, L. (1992). Petrology, elasticity, and composition of the mantle transition zone. *Journal of Geophysical Research* **97**, 6849–6866.

Iwamori, H., McKenzie, D. & Takahashi, E. (1995). Melt generation by isentropic mantle upwelling. *Earth and Planetary Science Letters* **134**, 253–266.

Jahn, B. M., Vidal, P. & Tilton, G. R. (1979). Archean mantle heterogeneity: evidence from chemical and isotopic abundances in Archean igneous rocks. *Philosophical Transactions of the Royal Society of London, Series A* **297**, 353–364.

Jahn, B. M., Gruau, G. & Glickson, A. Y. (1982). Komatiites of the Onverwacht Group, South Africa: REE chemistry, Sm–Nd age and mantle evolution. *Contributions to Mineralogy and Petrology* **80**, 25–40.

Jochum, K. P., Arndt, N. T. & Hofmann, A. W. (1991). Nb–Th–La in komatiites and basalts: constraints on komatiite petrogenesis and mantle evolution. *Earth and Planetary Science Letters* **107**, 272–289.

Kareem, K. (2005). Komatiites of the Weltevreden Formation, Barberton greenstone belt, South Africa: implications for the chemistry and temperature of the Archean mantle. Baton Rouge: PhD thesis, Lousiana State University, 204 pp.

Kato, T., Ohtani, E., Ito, Y. & Onuma, K. (1996). Element partitioning between silicate perovskites and calcic ultrabasic melt. *Physics of the Earth and Planetary Interiors* **96**, 201–207.

Kato, T., Ringwood, A. E. & Irifune, T. (1988). Experimental determination of element partitioning between silicate perovskites, garnets and liquids: constraints on early differentiation of the mantle. *Earth and Planetary Science Letters* **89**, 123–145.

Kerr, A., Marriner, G., Arndt, N. T., Tarney, J., Nivia, A., Saunders, A., Storey, M. J. & Duncan, R. A. (1995). The petrogenesis of Gorgona komatiites, picrites and basalts: new field, petrographic and geochemical constraints. *Lithos* **37**, 245–260.

Kinzler, R. J. & Grove, T. L. (1985). Crystallization and differentiation of Archean komatiite lavas from northeast Ontario: phase equilibrium and kinetic studies. *American Mineralogist* **70**, 40–51.

Lahaye, Y., Arndt, N., Byerly, G., Chauvel, C., Fourcade, S. & Gruau, G. (1995). The influence of alteration on the trace-element and Nd isotopic compositions of komatiites. *Chemical Geology* **126**, 43–64.

Langmuir, C. H., Bender, J. F., Bence, A. E., Hanson, G. N. & Taylor, S. R. (1977). Petrogenesis of basalts from the FAMOUS area: Mid-Atlantic Ridge. *Earth and Planetary Science Letters* **36**, 133–156.

Lee, C.-T. A., Luffi, P., Höink, T., Li, J., Dasgupta, R. & Hernlund, J. W. (2010). Upside-down differentiation and generation of a 'primordial' lower mantle. *Nature* **463**, doi:10.1038/nature08824.

Lowe, D. R. & Byerly, G. R. (1999). Stratigraphy of the west–central part of the Barberton Greenstone Belt, South Africa. In: Lowe, D. R. & Byerly, G. R. (eds) *Geological Evolution of the Barberton Greenstone Belt*. Boulder, CO: Geological Society of America, 329, pp. 1–36.

Lowe, D. R., Byerly, G. R., Martin, J., van Kranendonk, R. H. S. & Vickie, C. B. (2007). An overview of the geology of the Barberton Greenstone Belt and vicinity: implications for early crustal development. *Developments in Precambrian Geology* **329**, 481–526.

Maaløe, S. (1982). Geochemical aspects of permeability controlled partial melting and fractional crystallization. *Geochimica et Cosmochimica Acta* **46**, 43–57.

Matzen, A. K., Baker, M. B., Beckett, J. R. & Stolper, E. M. (2011). Fe–Mg partitioning between olivine and high-magnesian melts and the nature of Hawaiian parental liquids. *Journal of Petrology* **52**, 1243–1263.

McDonough, W. F. & Ireland, T. R. (1993). Intraplate origin of komatiites inferred from trace elements in glass inclusions. *Nature* **365**, 432–434.

McDonough, W. F. & Sun, S. s. (1995). The composition of the Earth. *Chemical Geology* **120**, 223–253.

McKenzie, D. & Bickle, M. J. (1988). The volume and composition of melt generated by extension of the lithosphere. *Journal of Petrology* **29**, 625–679.

Miller, G. H., Stolper, E. M. & Ahrens, T. J. (1991). The equation of state of a molten komatiite 2. Application to komatiite petrogenesis and the Hadean mantle. *Journal of Geophysical Research* **96**, 11849–11864.

Nesbitt, R. W., Sun, S. S. & Purvis, A. C. (1979). Komatiites: geochemistry and genesis. *Canadian Mineralogist* **17**, 165–186.

Nesbitt, R. W., Jahn, B. M. & Purvis, A. C. (1982). Komatiites: an early Precambrian phenomenon. *Journal of Volcanology and Geothermal Research* **14**, 31–45.

Nisbet, E. G. (1982). The tectonic setting and petrogenesis of komatiites. In: Arndt, N. T. & Nisbet, E. G. (eds) *Komatiites*. London: George Allen & Unwin, pp. 501–520.

Nisbet, E. G., Arndt, N. T., Bickle, M. J., Cameron, W. E., Chauvel, C., Cheadle, M., Hegner, E., Kyser, T. K., Martin, A., Renner, R. & Roedder, E. (1987). Uniquely fresh 2·7 Ga komatiites from the Belingwe greenstone belt, Zimbabwe. *Geology* **15**, 1147–1150.

Nisbet, E. G., Cheadle, M. J., Arndt, N. T. & Bickle, M. J. (1993). Constraining the potential temperature of the Archaean mantle: A review of the evidence from komatiites. *Lithos* **30**, 291–307.

Ohtani, E. (1984). Generation of komatiite magma and gravitational differentiation in the deep upper mantle. *Earth and Planetary Science Letters* **67**, 261–272.

Ohtani, E., Kawabe, I., Moriyama, J. & Nagata, Y. (1989). Partitioning of elements between majorite garnet and melt and implications for petrogenesis of komatiite. *Contributions to Mineralogy and Petrology* **103**, 263–269.

Parman, S. W., Dann, J. C., Grove, T. L. & de Wit, M. J. (1997). Emplacement conditions of komatiite magmas from the 3·49 Ga Komati Formation, Barberton Greenstone Belt, South Africa. *Earth and Planetary Science Letters* **150**, 303–323.

Parman, S., Grove, T. L. & Dann, J. (2001). The production of Barberton komatiites in an Archean subduction zone. *Geophysical Research Letters* **28**, 2513–2516.

Parman, S. W., Shimizu, N. & Grove, T. L. (2003). Constraints on the pre-metamorphic trace element composition of Barberton komatiites from ion probe analyses of preserved clinopyroxene. *Contributions to Mineralogy and Petrology* **144**, 383–396.

Parman, S. W., Grove, T. L., Dann, J. C. & de Wit, M. J. (2004). A subduction origin for komatiites and cratonic lithospheric mantle. *South African Journal of Geology* **107**, 107–118.

Pyke, D. R., Naldrett, A. J. & Eckstrand, O. R. (1973). Archean ultramafic flows in Munro Township, Ontario. *Geological Society of America Bulletin* **84**, 955–978.

Révillon, S., Arndt, N. T., Chauvel, C. & Hallot, E. (2000). Geochemical study of ultramafic volcanic and plutonic rocks from Gorgona Island, Colombia: the plumbing system of an oceanic plateau. *Journal of Petrology* **41**, 1127–1153.

Richter, F. M. (1988). A major change in the thermal state of the Earth at the Archean–Proterozoic boundary: consequences for the nature and preservation of continental lithosphere. *Journal of Petrology* **Special Volume**, 39–52.

Rigden, S. M., Ahrens, T. J. & Stolper, E. M. (1988). Shock compression of molten silicate: results for a model basaltic composition. *Journal of Geophysical Research* **93**, 367–382.

Sakamaki, T., Ohtani, E., Urakawa, S., Suzuki, A. & Katayama, Y. (2010). Density of dry peridotite magma at high pressure by X-ray absorption method. *American Mineralogist* **95**, 144–147.

Salters, V. J. M. & Stracke, A. (2004). Composition of the depleted mantle. *Geochemistry, Geophysics, Geosystems* **5**, Q05B07.

Shaw, D. M. (1970). Trace element fractionation during anatexis. *Geochimica et Cosmochimica Acta* **34**, 237–243.

Shimizu, K. T., Komiya, S., Maruyama, S. & Hirose, K. (2001). Water content of melt inclusion in Cr-spinel of 2.7 Ga komatiite from Belingwe Greenstone Belt, Zimbabwe. *Earth and Planetary Science Letters* **78**, 750.

Smith, H. S., Erlank, A. J. & Duncan, A. R. (1980). Geochemistry of some ultramafic komatiite lava flows from the Barberton Mountain Land, South Africa. *Precambrian Research* **11**, 399–415.

Smith, H. S. & Erlank, A. J. (1982). Geochemistry and petrogenesis of komatiites from the Barberton greenstone belt, South Africa. In: Arndt, N. T. & Nisbet, E. G. (eds) *Komatiites*. London: George Allen & Unwin, pp. 347–398.

Sobolev, A. V., Hofmann, A. W., Kuzmin, D. V., Yaxley, G. M., Arndt, N. T., Chung, S.-L., Danyushevsky, L. V., Elliott, T., Frey, F. A., Garcia, M. O., Gurenko, A. A., Kamenetsky, V. S., Kerr, A. C., Krivolutskaya, N. A., Matvienkov, V. V., Nikogosian, I. K., Rocholl, A., Sigurdsson, I. A., Sushchevskaya, N. M. & Teklay, M. (2007). The amount of recycled crust in sources of mantle-derived melts. *Science* **316**, 412–417.

Stiegler, M. T., Lowe, D. R. & Byerly, G. R. (2008). Abundant pyroclastic komatiitic volcanism in the 3·5 to 3·2 Ga Barberton greenstone belt, South Africa. *Geology* **36**, 779–782.

Stiegler, M. T., Lowe, D. R. & Byerly, G. R. (2010). The petrogenesis of volcaniclastic komatiites in the Barberton Greenstone Belt, South Africa: a textural and geochemical study. *Journal of Petrology* **51**, 947–972.

Stixrude, L. & Lithgow-Bertelloni, C. (2010). Thermodynamics of the Earth's mantle. *Reviews in Mineralogy and Geochemistry* **71**, 465–483.

Sun, S. S. & Nesbitt, R. W. (1978). Petrogenesis of Archaean ultrabasic and basic volcanics: Evidence from rare earth elements. *Contributions to Mineralogy and Petrology* **65**, 301–325.

Suzuki, A., Ohtani, E. & Kato, T. (1998). Density and thermal expansion of a peridotite melt at high pressure. *Physics of the Earth and Planetary Interiors* **107**, 53–61.

Takahashi, E. (1986). Melting of a dry peridotite KLB-1 up to 14 GPa: implications on the origin of peridotitic upper mantle. *Journal of Geophysical Research* **91**, 9367–9382.

Taura, H., Yurimoto, H., Kato, T. & Sueno, S. (2001). Trace element partitioning between silicate perovskites and ultracalcic melt. *Physics of the Earth and Planetary Interiors* **124**, 25–32.

Thompson, M. E., Kareem, K. M., Xie, X. & Byerly, G. R. (2003). Fresh melt inclusions in 3·3 Ga komatiitic olivines from the Barberton greenstone belt, South Africa. *Lunar and Planetary Science*, abstract No 2112.

Veizer, J. (1988). Continental growth: Comments on 'The Archean–Proterozoic transition: Evidence from Guyana and Montana'. In: Gibbs, A. K., Montgomery, C. W., O'Day, P. A. & Erslev, E. A. (eds). *Geochimica et Cosmochimica Acta* **52**, 789–792.

Viljoen, M. J. & Viljoen, R. P. (1969a). The geology and geochemistry of the Lower Ultramafic Unit of the Onverwacht Group and a proposed new class of igneous rock. *Geological Society of South Africa, Special Publication* **2**, 55–86.

Viljoen, M. J. & Viljoen, R. P. (1969b). Evidence for the existence of a mobile extrusive peridotitic magma from the Komati Formation of the Onverwacht Group. *Geological Society of South Africa, Special Publication* **2**, 87–112.

Viljoen, R. P. & Viljoen, M. J. (1969c). The effects of metamorphism and serpentinisation on the volcanic and associated rocks of the Barberton region. *Geological Society of South Africa, Special Publication* **2**, 29–54.

Viljoen, M. J., Viljoen, R. P., Smith, H. S. & Erlank, A. J. (1983). Geological, textural and geochemical features of komatiitic flows from the Komati Formation. *Geological Society of South Africa* **9(Special Publication)**, 1–20.

Walter, M. J. (1998). Melting of garnet peridotite and the origin of komatiite and depleted lithosphere. *Journal of Petrology* **39**, 29–60.

Williams, D. A. & Furnell, R. G. (1979). Reassessment of part of the Barberton type area. *Precambrian Research* **9**, 325–347.

Wilson, A. H. (1979). A new class of silica enriched, highly depleted komatiites in the southern Kaapvaal Craton, South Africa. *Precambrian Research* **127**, 125–141.

Wuth, M. G. (1980). The geology and mineralization potential of the Oorschot–Weltevreden Schist Belt south-west of Barberton, eastern Transvaal. PhD thesis, Johannesburg: Witwatersrand University.

Xie, Q., Kerrich, R. & Fan, J. (1993). HFSE/REE fractionations recorded in three komatiite–basalt sequences, Archean Abitibi greenstone belt: Implications for multiple plume sources and depths. *Geochimica et Cosmochimica Acta* **57**, 4111–4118.

Zhang, J. & Herzberg, C. (1994). Melting experiments on anhydrous peridotite KLB-1 from 5·0 to 22·5 GPa. *Journal of Geophysical Research* **99**, 17729–17742.